The Cryosphere

Impact of snow thermal conductivity schemes on pan-Arctic permafrost dynamics in the Community Land Model version 5.0

Adrien Damseaux[1,2,3], Heidrun Matthes[1], Victoria R. Dutch[4,5], Leanne Wake[5], and Nick Rutter[5]

[1]Alfred-Wegener-Insitut (AWI), Potsdam, Germany
[2]Karlsruhe Institute of Technology (KIT), IMK-IFU, Garmisch-Partenkirchen, Germany
[3]Institute of Physics and Astronomy, University of Potsdam, Potsdam, Germany
[4]School of Environmental Sciences, University of East Anglia, Norwich, UK
[5]Department of Geography and Environmental Sciences, Northumbria University, Newcastle, UK

Correspondence: Adrien Damseaux (adrien.damseaux@kit.edu)

Abstract. The precise magnitude and timing of permafrost-thaw-related emissions and their subsequent impact on the global climate system remain highly uncertain. This uncertainty stems from the complex quantification of the rate and extent of permafrost thaw, which is influenced by factors such as snow cover and other surface properties. Acting as a thermal insulator, snow cover directly influences surface energy fluxes and can significantly impact the permafrost thermal regime. However, current Earth system models often inadequately represent the nuanced effects of snow cover in permafrost regions, leading to inaccuracies in simulating soil temperatures and permafrost dynamics. Notably, the Community Land Model (CLM5.0) tends to overestimate snowpack thermal conductivity over permafrost regions, resulting in an underestimation of the snow insulating capacity. Using a snow thermal conductivity scheme better adapted for the snowpack typically found in permafrost regions, we seek to resolve thermal insulation underestimation and assess the influence of snow on simulated soil temperatures and permafrost dynamics. Evaluation using two Arctic-wide soil temperature observation datasets reveals that the new snow thermal conductivity scheme reduces the cold-soil temperature bias (root-mean-square error, RMSE $= 3.17$ to $2.4\,°C$, using remote sensing data; RMSE $= 3.9$ to $2.19\,°C$, using in situ data), demonstrates robustness through sensitivity analysis under lower tundra snow densities, and addresses the overestimation of permafrost extent in the default CLM5.0. This improvement highlights the importance of incorporating realistic snow processes in land surface models for enhanced predictions of permafrost dynamics and their response to climate change.

1 Introduction

Permafrost contains between 677 and 949 Pg of soil organic carbon (SOC) in the upper few metres, roughly twice as much carbon as the atmosphere (Palmtag et al., 2022). As permafrost thaws with increased temperature, SOC becomes available for microbial decomposition, resulting in the release of large amounts of greenhouse gases into the atmosphere, which, in turn, increase surface temperatures. This permafrost–carbon feedback will likely accelerate climate change; however, the precise magnitude and timing of these emissions and their subsequent impact on the global climate system remain uncertain (Schuur et al., 2015).

A key aspect of this uncertainty is the complex quantification of the rate and extent of permafrost thaw. Predicting how the permafrost thermal regime will respond to ongoing climate change is particularly challenging, given its high sensitivity to surface properties (Barrere et al., 2017). Among these, snow cover acts as an important moderator by directly influencing surface energy fluxes between the air and the soil. Functioning as a thermal insulator, snow cover can limit heat loss from the ground during winter (Lawrence and Slater, 2010; Li et al., 2021; Royer et al., 2021), but its insulating properties are highly variable and insufficiently detailed in Earth system models (Barrere et al., 2017).

The insulating efficiency of snow cover increases with thickness, reaching its peak insulation capacity at around 25 cm in depth (Slater et al., 2017) depending on the (micro)structure and stratigraphy of the snowpack. As denser snow has fewer air voids, resulting in fewer insulating air pockets, thermal conductivity also tends to increase with density (Adams and Sato, 1993). As a result, heat is transferred more efficiently through a dense snow matrix. Snowpack in Arctic tundra environments typically consists of two main parts: depth hoar and wind slab (Sturm et al., 1995; Domine et al., 2018). Depth hoar forms towards the base of the snowpack due to strong vertical temperature gradients and water vapour fluxes. Wind slab forms due to snow compaction from the strong Arctic wind transport and deposition. Depth hoar crystals have large, faceted, and often cup-shaped grains with low density, making them poor heat conductors, while wind slab layers have higher density, resulting in better heat conductivity and decreased insulation properties.

Studies show that state-of-the-art land surface models (LSMs) and snowpack models, including the Community Land Model (CLM5.0; Lawrence et al., 2019), Crocus (Vionnet et al., 2012), and SNOWPACK (Bartelt and Lehning, 2002), struggle to represent these two phenomena (Barrere et al., 2017; Gouttevin et al., 2018; Domine et al., 2019; Dutch et al., 2022; Schädel et al., 2024). Notably, vertical density profiles simulated by these models often exhibit significant discrepancies compared to observed snow density, in both the top wind slab and bottom depth hoar layers of the snowpack (Dutch et al., 2022). Efforts such as those by Brondex et al. (2023) aim to address this issue by developing finite-element models to improve the representation of interactions between heat conduction and water vapour diffusion in snowpack models. However, this extensive work is still in early stages, and neglecting the role of depth hoar in providing thermal insulation properties to Arctic tundra snowpacks can have large consequences for soil temperature representation within LSMs (Gouttevin et al., 2018; Royer et al., 2021; Dutch et al., 2022).

The insulating capacity of a snowpack is determined by the snow thermal conductivity: a critical parameter influencing heat exchange between the soil and atmosphere. Previous studies have highlighted the high sensitivity of LSM soil temperature simulations to this parameter (Wang et al., 2013; Paquin and Sushama, 2015), identifying it as a significant source of uncertainty (Langer et al., 2013; Barrere et al., 2017; Domine et al., 2019; Hu et al., 2023). In models, it is expressed as the effective snow thermal conductivity K_{eff}, which aims to account for all heat-transfer processes in a single vertical dimension. Snow exhibits a low K_{eff}, generally falling within the range of 0.01–0.7 $\mathrm{W\,m^{-1}\,K^{-1}}$ (Gouttevin et al., 2018); tundra snowpacks typically display K_{eff} values toward the lower end of this range (Sturm et al., 1997; Domine et al., 2016; Dutch et al., 2022). Numerous studies (Yen, 1981; Jordan, 1991; Sturm et al., 1997; Calonne et al., 2011; Fourteau et al., 2021) describe empirical relationships between K_{eff} and snow density based on experiments made in laboratories on different snowpacks around the world. Among them, Sturm et al. (1997) derived a regression equation relating density and thermal conductivity based on 488 measurements of pan-Arctic and Antarctic seasonal snow:

$$K_{eff} = \begin{cases} 0.023 + 2.23 \times 10^{-4} \cdot \rho_{sno} , & \text{if } \rho_{sno} < 156 \\ 0.138 - 1.01 \times 10^{-3} \cdot \rho_{sno} & \text{if } 156 \leq \rho_{sno} \\ +3.233 \times 10^{-6} \cdot \rho_{sno}^2 , & \leq 600 \end{cases} , \quad (1)$$

where ρ_{sno} is the snow density (in $\mathrm{kg\,m^{-3}}$). The Sturm equation stands out due to its notably lower K_{eff} compared to other relationships based on non-Arctic snowpacks (Fig. A1), particularly within the range of typical Arctic tundra snowpack densities, 150 to 300 $\mathrm{kg\,m^{-3}}$.

Barrere et al. (2017) demonstrate that the Sturm et al. (1997) equation better fits their measurements in the Qarlikturvik Valley because it is specifically based on tundra snow characteristics. In contrast, equations commonly used by many LSMs (e.g. the Anderson (1976) equation in ORCHIDEE (Guimberteau et al., 2018), the Mellor (1977) equation in CLASSIC1.0 (Melton et al., 2020), the Yen (1981) equation in ISBA (Boone et al., 2016) and JULES (Best et al., 2011), and the Jordan (1991) equation in CLM5 and ELMv0 (Golaz et al., 2019)) are more adapted to alpine conditions and may not accurately represent pan-Arctic environments. Royer et al. (2021) conducted a sensitivity experiment involving five modified settings in Crocus, one of which incorporated the Sturm et al. (1997) equation. Their assessment demonstrated only slight improvements in soil temperature; however, it is difficult to isolate the specific impact of the Sturm et al. (1997) equation in their study amongst the other modified parameters. Conversely, Dutch et al. (2022) conducted a comparative analysis of different snow thermal conductivity schemes with CLM5.0 using in situ measurements from Trail Valley Creek, Northwest Territories, Canada, and found that the CLM5.0 default scheme (Jordan, 1991) overestimates snow thermal conductivity by a factor of 3 compared to observations, consequently inducing a cold bias in the wintertime soil temperature simulations. When replacing the default scheme with the formulation proposed by Sturm et al. (1997), significant improvements were observed in wintertime soil temperature simulations. In addition, Paquin and Sushama (2015) and Tao et al. (2024) studied the effects of integrating the Sturm et al. (1997) equation into the LSMs CLASS (Verseghy, 1991) and ELM (Golaz et al., 2019), respectively, further underscoring the significant sensitivity of soil temperatures to snow thermal conductivity. Moreover, Paquin and Sushama (2015) demonstrate that the Sturm et al. (1997) scheme effectively mitigates winter soil temperature biases.

Our study aims to extend the Dutch et al. (2022) assessment to evaluate the applicability of the Sturm et al. (1997) scheme in CLM5.0 across a broader regional climatological context. We hypothesise that a modification to the CLM5.0

snow thermal conductivity scheme will more effectively capture the sensitivity inherent in Arctic tundra snow, thereby restoring a more accurate thermal insulating function of the snowpack and improving the soil temperature and permafrost dynamics represented by the model. To realise this endeavour, we present a CLM5.0 sensitivity experiment using the Sturm et al. (1997) snow thermal conductivity scheme and evaluate simulations using Arctic-wide in situ observations and remote sensing data for soil temperature. Additionally, we conduct a sensitivity analysis of snow density to test the robustness of our results for potentially lower bulk snow densities characteristic of tundra environments.

2 Methods and data

2.1 Model description

This study uses the Community Land Model (CLM5.0), which is part of the Community Terrestrial Systems Model (CTSM; https://github.com/ESCOMP/CTSM, last access: 8 April 2025). CLM5.0 is released by the National Center for Atmosphere Research (NCAR) and is the default land component of the community-developed Earth system model CESM2. CLM5.0 is a process-based model of the land surface and the terrestrial biosphere that calculates water, energy, and carbon fluxes between the surface and different soil layers. A comprehensive model description and global evaluation can be found in Lawrence et al. (2019) and in the technical description (Lawrence et al., 2018).

2.1.1 Soil

The model soil stratigraphy includes 25 soil layers distributed geometrically, with thinner layers at shallower depths and larger layers at greater depths up to -50 m. CLM5.0 has an increased soil layer resolution compared to CLM4.5, particularly in the upper -3 m, to more accurately represent the active-layer thickness (ALT) in permafrost areas (Lawrence et al., 2019).

The heat-transfer equation Lawrence et al. (Eq. 6.4; 2018) is numerically solved to compute soil temperatures across the 25-layer column, assuming a heat flux of zero at the bottom of the soil column. Soil temperatures are evaluated at each time step to assess phase changes in water and account for latent heat uptake and release. Hydrological calculations are conducted in the upper 20 soil layers, while the 5 bedrock layers are impermeable to water. Vertical soil moisture transport in the model is driven by the water balance equation of the whole column system, considering infiltration, surface and subsurface runoff, gradient diffusion, gravity, canopy transpiration through root extraction, and interactions with groundwater, respecting the conservation of mass. Vertical soil water flux is computed using Darcy's law.

The model defines soil thermal and hydraulic conductivities using mineral soil parameterisations dependent on soil texture (sand, clay, and silt fractions) and organic matter density derived from Hugelius et al. (2013). These fractions vary across the first 10 layers but remain constant in the subsequent 15 layers.

2.1.2 Snow

The snow module in CLM5.0, described in van Kampenhout et al. (2017) and Lawrence et al. (2019), includes physical processes such as snow accumulation, compaction (due to overburden pressure and drifting snow), refreezing, melting, and sublimation. However, the snow module does not take into account water vapour flux through snow. The CLM5.0 snow module uses a multi-layer approach that discretises the snowpack into a maximum of 12 layers. Fresh-snow density is parameterised by combining a temperature term with a linear wind-dependent density term (van Kampenhout et al., 2017). Snow can densify via four distinct processes: compaction by overburden pressure, compaction by drifting snow, destructive metamorphism, or melt metamorphism. Furthermore, snow thermal conductivity is solely dependent on snow density and is calculated following the Jordan (1991) scheme by default:

$$K_{eff} = \lambda_{air} + \left(7.75 \times 10^{-5} \rho_{sno} + 1.105 \times 10^{-6} \rho_{sno}^2\right) \times (\lambda_{ice} - \lambda_{air}), \tag{2}$$

where λ_{air} and λ_{ice} are the thermal conductivity of air, 0.023 W m^{-1} K^{-1}, and ice, 2.29 W m^{-1} K^{-1}, respectively. Improvements to the CLM5.0 snow module have led to increased bulk snow density across most of the Arctic tundra compared to CLM4.5 (Lawrence et al., 2019).

2.2 Model set-up and experiments

The version of CLM used throughout this study is ctsm5.1.dev086. The domain for this study is between 57 and $90°$ N and consists of 204 086 grid points with a triangular resolution that varies between 116.3 and 179.4 km^2, giving a rectangular resolution of around 12 km^2. This is a similar domain to that of Birch et al. (2020), who used a coarser resolution.

Default CLM5.0 meteorological forcing data (CRU/GSWP3) are replaced with the finer 31 km^2 spatial resolution ERA5 forcings from 1980 to 2021 (Hersbach et al., 2020) at an hourly time step. To our knowledge, this is the second time that CLM5.0 has been used with ERA5 forcings, after Cheng et al. (2023). While this increase in resolution should represent a substantial improvement over previous global reanalysis methods used (Albergel et al., 2018), it also introduces additional uncertainty since the model was not parameterised with these settings as its default configuration. To start the run in an equilibrium state, a spin-up of 30 years using the ERA5 reanalysis (looping from 1980 to 1989 three times) was done before running the model from 1980 to 2021 (42 years).

To reduce computation time, this study uses the satellite phenology (SP) set-up, which does not include complex carbon cycle interactions and deactivates the land–ice and river routing models. In order to prevent unrealistically high values of snow heights observed in pan-Arctic non-glaciated islands, the snow initialisation protocol was recalibrated with the snow water equivalent (SWE) reverted to its original value of 0.8 m, instead of 10 m as was later proposed in van Kampenhout et al. (2017).

We conducted two simulations: (1) the control run and (2) the Sturm run, where the conventional snow thermal conductivity scheme is replaced with the Sturm et al. (1997) scheme (Eq. 1). To assess the sensitivity of model outputs to snow density, additional simulations were performed using both the Sturm and Jordan thermal conductivity schemes, with adjustment factors of 0.9 and 0.7 applied to the snow density parameterisation to better represent the lower bulk snow densities characteristic of tundra environments. In CLM5.0, the snow density is computed as follows:

$$\rho_{sno} = af \cdot \left(\frac{\omega_{ice} + \omega_{liq}}{frac_{snow} \cdot d_z} \right), \qquad (3)$$

where af is the adjustment factor used in this sensitivity analysis, ω_{ice} is the ice lens mass per unit area (in $kg\,m^{-2}$), ω_{liq} is the liquid water mass per unit area (in $kg\,m^{-2}$), $frac_{snow}$ is the fractional snow-covered area, and d_z is the snow layer depth (in m).

The choice of adjustment factors is based on observed snow density values in Arctic tundra regions. CLM5.0 simulates an average bulk snow density of $311\,kg\,m^{-3}$ over our study domain (Fig. A2), whereas observational studies indicate that tundra snow densities should be significantly lower. Zhao et al. (2023) reported an average tundra bulk snow density of $225\,kg\,m^{-3}$ using a large dataset of Arctic-wide snow sites, while depth hoar density measurements from multisite (Derksen et al., 2014) and single-site studies (Woolley et al., 2024) both report values around $228\,kg\,m^{-3}$. To align model outputs with these observations, an af of 0.7 was chosen to represent the lower range of observed densities, yielding a modelled bulk snow density of $217\,kg\,m^{-3}$. Additionally, an af of 0.9 was selected as an intermediate value between the CLM5.0 simulated densities and the observed tundra densities.

The simulations were conducted exclusively for the 2006–2010 period, selected due to its robust observational data availability, to balance computational efficiency with model reliability. The four additional runs include (1) Sturm with af = 0.9, (2) Jordan with af = 0.9, (3) Sturm with af = 0.7, and (4) Jordan with af = 0.7. These sensitivity runs were compared to the baseline simulations (with af = 1.0) as part of a broader analysis of snow density impacts on model performance.

2.3 Data for model evaluation

The Arctic tundra has long been recognised as a difficult region to study due to its inherent remoteness and the scarcity of observations (Matthes et al., 2017; Domine et al., 2019; Royer et al., 2021). Accordingly, the lack of information on snow properties in Arctic tundra regions places a major limitation on permafrost and climate modelling (Domine et al., 2016; Gouttevin et al., 2018). To address this challenge, this paper uses two observation datasets as constraints for the CLM5.0 outputs: one derived from remote sensing products and the other obtained through in situ measurements. Both datasets offer complementary perspectives, enabling a thorough integration and analysis of soil temperature assessment, including (1) temporal-scale variations covering seasonal and annual averages, (2) spatial distributions across a wide geographical area, and (3) depth variations throughout the entire soil column.

2.3.1 Remote sensing data

We use grid-based products from the European Space Agency (ESA) Climate Change Initiative (CCI) Essential Climate Variables (ECVs) product database from the CCI+ Permafrost project (Obu et al., 2024). ESA-CCI products encompass ECVs with a high spatial resolution of $1\,km^2$ and include mean annual ground temperature (MAGT) at distinct ground depths of 1, 5, and 10 m; permafrost fraction (PFR) – proportion of an area covered by permafrost within a grid point; and the ALT – the top layer of soil that thaws during the warm season and freezes during the colder months. Product validation is documented in Heim et al. (2021), with further details on the methods available in Obu et al. (2019). The geographical extent of these products spans the Northern Hemisphere above 30° N within an Arctic stereographic circumpolar projection. The temporal coverage for the MAGT, ALT, and PFR time series is from 1997 to 2019 at an annual resolution.

To compare CLM5.0 simulations to ESA-CCI products, we aggregated ESA-CCI products to the domain grid using a conservative second-order regridding equation described in Jones (1999). Following the Osterkamp and Romanovsky (1999) definition of permafrost as ground that remains at or below 0 °C for at least 2 consecutive years, the presence or absence of permafrost (PFR) at each grid point within CLM5.0 is determined by

$$PFR = \begin{cases} 1, & \frac{1}{M}\sum_{y=1}^{M} \min_{z=1,N} \max_{t(y)=1,2Y} T_i(z,t(y)) \\ & < 273.15\,K \\ 0, & \frac{1}{M}\sum_{y=1}^{M} \min_{z=1,N} \max_{t(y)=1,2Y} T_i(z,t(y)) \\ & \geq 273.15\,K \end{cases}, \qquad (4)$$

where M is the number of years covered by ESA-CCI product (1997–2019), z is the index for the soil depth, N is the number of depths, t is the index for the days in the year y and the next year ($y + 1$), Y is the number of days in a year, and

$T_i(z, (t(y)))$ is the temperature depending on the day, depth, and grid cell. We first calculated the maximum temperature over a 2-year period for each grid cell and each layer. Then, we calculated the vertical soil temperature minimum to see if there is one continually frozen layer over these 2 years. From this, we obtained a temperature data grid for each year, which we then averaged over the period spanning 1997 to 2019 to match the duration of the ESA-CCI product period. Subsequently, we classified grid points into two categories: those with temperatures below 0 °C were designated permafrost, while those with temperatures above 0 °C were classified as non-permafrost. It is worth noting that this method provides a binary definition of permafrost, in contrast to the ESA-CCI classification, which offers a quantitative representation of permafrost ranging from 0 % to 100 % resulting from their ensemble-member experiments. To reconcile this difference, we adopted three permafrost classes for the ESA-CCI data: continuous if greater than 90 %, discontinuous if between 50 % and 90 %, and permafrost-free if less than 50 %.

To calculate ALT at each grid point within CLM5.0 for each year, a grid of maximum annual soil temperature was computed to identify the first thawed layer (above 0 °C) from the basal layer. Subsequently, a spline curve was calculated using the layers above and below the first thawed layer to estimate the actual depth of transition between frozen and thawed soil layers. The resulting ALTs for both CLM5.0 and ESA-CCI were then averaged between 1997 and 2019.

To obtain the maps presented in the results section, we subtracted the ESA-CCI grid data from the CLM5.0 simulations for the MAGT, PFR, and ALT period-averaged products. In addition, we calculated the mean absolute deviation (MAD) and root-mean-square error (RMSE) for MAGT and ALT, where predicted values are the results from the model and observed values are the ESA-CCI products.

2.3.2 In situ soil temperatures

We expanded upon the dataset used by Matthes et al. (2017) using data from the Permafrost Laboratory website (https://permafrost.gi.alaska.edu, last access: 8 April 2025), the GTN-P database (http://gtnpdatabase.org, last access: 8 April 2025), the Nordicana D website (https://nordicana.cen.ulaval.ca/, last access: 8 April 2025), and the Roshydromet network (http://meteo.ru/data/, last access: 8 April 2025). The resulting database, denoted herein 295GT, comprises monthly average temperatures for 295 borehole stations over 42 years, from 1980 to 2021, across the entire Arctic (Fig. 1). Soil temperatures have been recorded across 278 distinct depth levels, ranging from −0.01 to −60 m. When comparing the model results with the 295GT dataset, each station is matched with the nearest grid point, and a linear interpolation is performed using the two closest CLM5.0 depth level options.
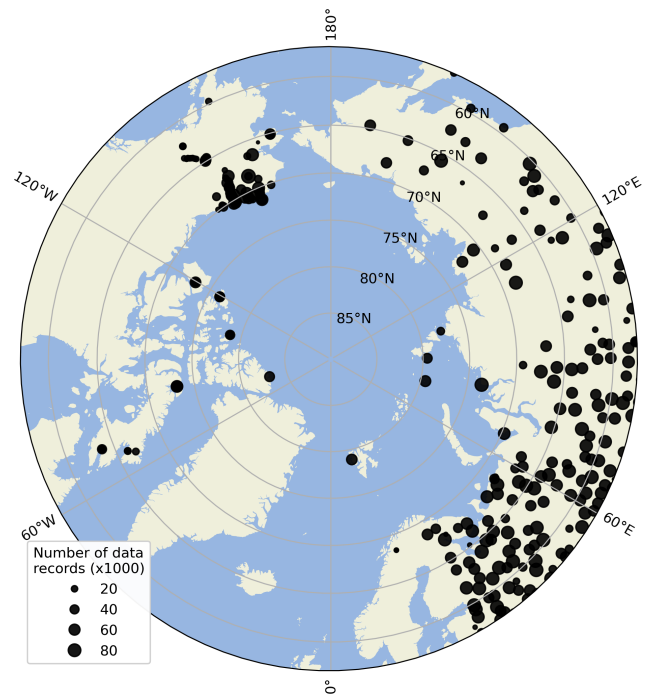
Figure 1. Locations of the 295 borehole stations used. The size of each point represents the number of data records per station over the whole period and for all depths. The datasets are sourced from the Permafrost Laboratory website, the GTN-P database, Nordicana D, and the Roshydromet network.

3 Results

3.1 Snow insulation

The winter offset, as defined by Burke et al. (2020), quantifies the difference between the mean soil temperature at 0.2 m and the mean air temperature during the December to February period. This metric provides valuable insight into the snow insulation capacity and the transfer of heat from the air to the soil during the winter season as represented by an LSM.

The Sturm run demonstrates substantially higher snow insulation across most of the domain, notably in tundra regions, when compared to the control run (Fig. 2). Offset values range from 20 to 35 °C over Siberia and 15 to 25 °C over Canada and Alaska for the Sturm run compared to 10 to 20 °C over most regions for the control run.

Following the methodology outlined by Wang et al. (2016), Fig. 3 illustrates the snow insulation effect between the control and Sturm runs across the 295GT Russian site locations ($n = 178$), with colours representing various temperature regimes. The disparity in results between the runs is most notable in the cold-temperature regime (tundra regions), where the winter offset linearly increases up to 40 cm in snow depth and stabilises thereafter in the Sturm run. Conversely, the relationship between snow depth and
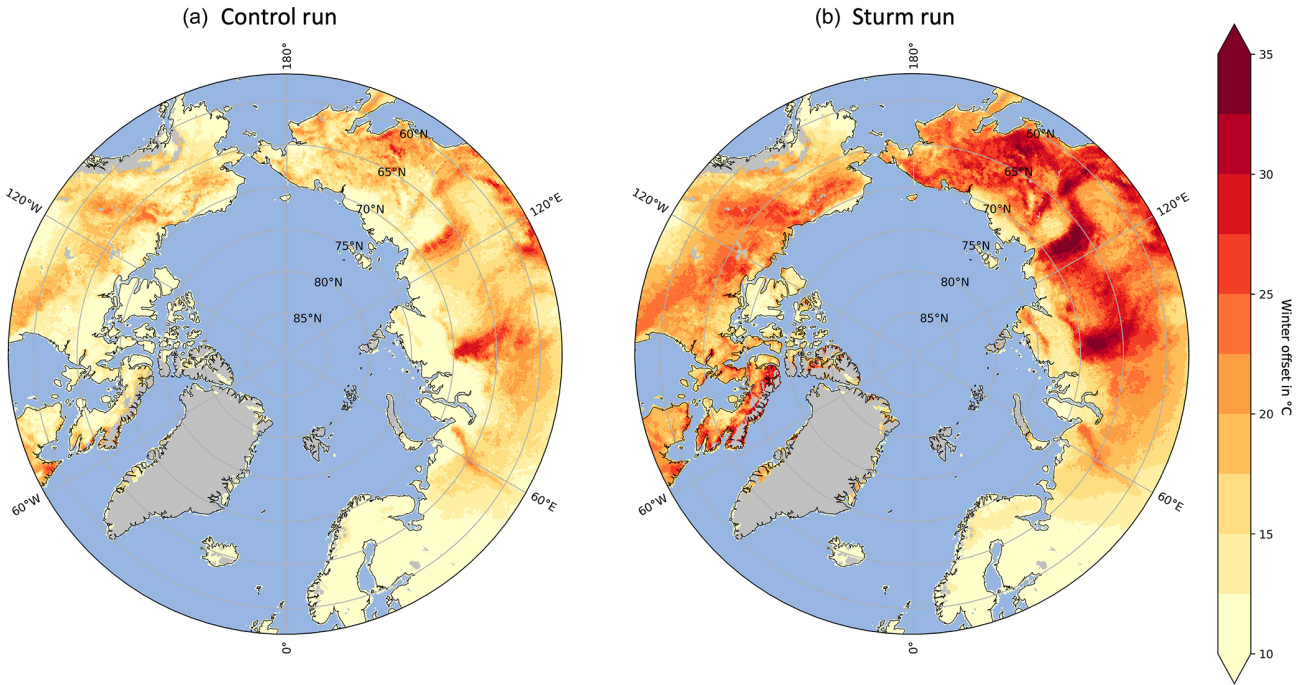
Figure 2. Period-averaged (1980 to 2021) winter offset for the control run **(a)** and Sturm run **(b)**, following the Burke et al. (2020) methodology.
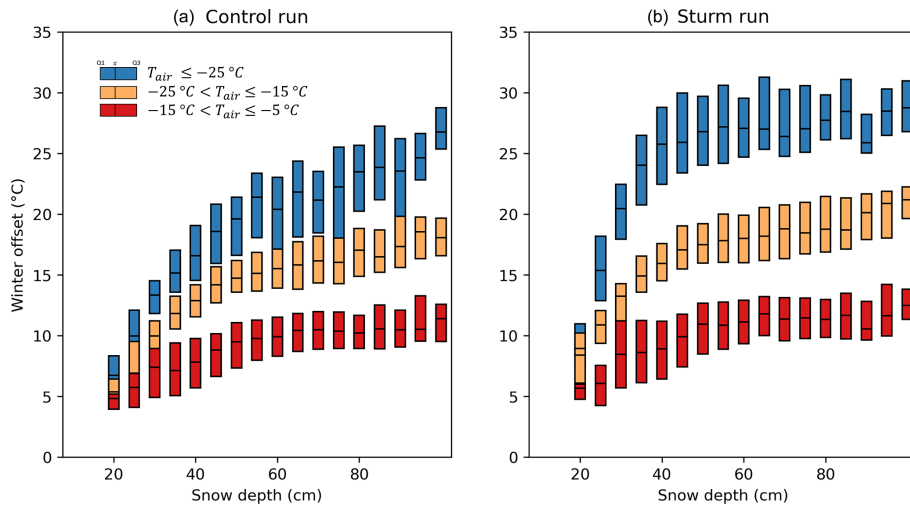
Figure 3. Variations in the winter offset according to snow depth between the control **(a)** and Sturm **(b)** runs calculated from the 295GT Russian site locations ($n = 178$) and 41 individual winters (1981–2021), following a methodology similar to the model comparison undertaken by Wang et al. (2016). Each box plot represents 5 cm snow depth bins, and colours indicate different air temperature regimes.

winter offset is close to linear across all snow depths in the control run.

3.2 Soil temperature

Our initial hypothesis suggests that the cold bias in the control run is caused by the Jordan scheme's limitations in associating snow density with thermal conductivity under Arctic conditions, leading to higher-than-expected thermal conduc-

tivities that result in lower ground temperatures. To rectify this cold bias, we replaced the Jordan scheme with the Sturm scheme in the Sturm run, aiming to test whether this adjustment can improve the model's representation of ground temperature.
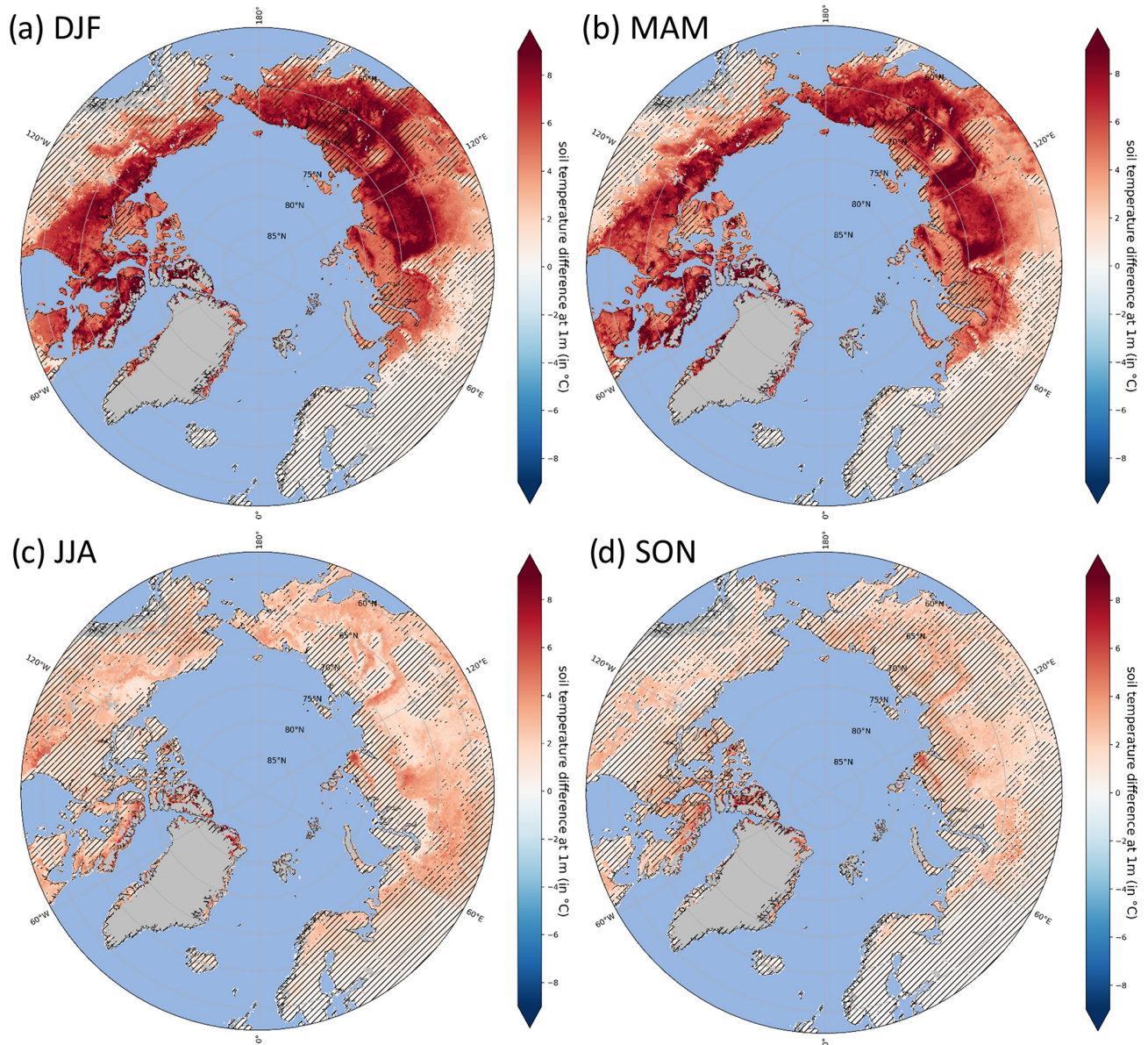
Figure 4. Period-averaged (1980–2021) soil temperature differences between the Sturm and control runs at -1 m in depth for four seasons: **(a)** December, January, and February (DJF); **(b)** March, April, and May (MAM); **(c)** June, July, and August (JJA); and **(d)** September, October, and November (SON). Darker red indicates that the Sturm run is warmer than the control run. The grey mask represents glaciers. Hatched areas represent non-significant results compared to the time series (p values < 0.95).

3.2.1 Comparison between the Sturm and control runs

During DJF, a significant temperature increase is observed in the Sturm run when compared to the control run (Fig. 4). In the Siberian permafrost region, temperatures increase by 4 to 10 °C, while in northern Canada and Alaska, they rise by up to 5 °C. In MAM, there is an increase of up to 3 °C found mostly over high-altitude areas across the whole domain and on the southwestern side of Hudson Bay. In JJA and SON, the increase in temperature is much less marked over the whole domain with an increase in temperature from 1 to 2 °C, ex-

cept for mountainous areas and the western Hudson Bay. In general, we observed a substantial increase in soil temperature in DJF and MAM when snow cover is important. This outcome aligns with our hypothesis that the increased snow insulation in the Sturm run would result in higher DJF soil temperatures.
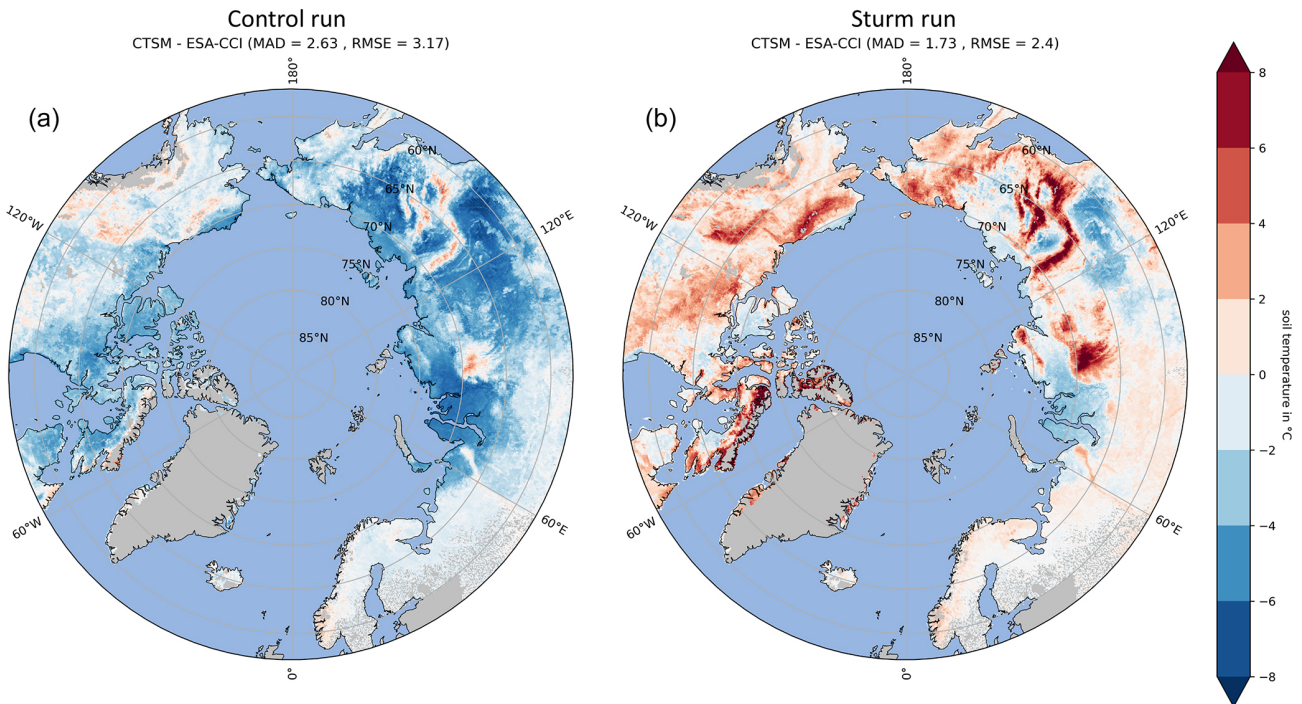
Figure 5. Period-averaged (1997 to 2019) MAGT at -1 m depth, with the difference between CTSM and ESA-CCI in °C for the control run **(a)** and the Sturm run **(b)**. Darker blue indicates that CTSM soil temperature is colder than ESA-CCI. ESA-CCI data are aggregated on the CTSM grid using a conservative second-order regridding method.

3.2.2 Comparison between the Sturm run and ESA-CCI

The evaluation of the -1 m year-averaged soil temperature (Fig. 5) compares results from the control and Sturm runs against the ESA-CCI dataset. The Sturm run significantly reduces the cold bias observed in the control run within tundra regions, including the West Siberian Plain, Central Siberian Plateau, Yakutsk Basin, Kolyma Lowland, and northern Canada. Similar improvements were observed at soil depths of -5 and -10 m (not shown here). Most regions only have a small cold bias of up to 2 °C.

The MAD and the spread of the temperature (RMSE) show a noteworthy improvement, decreasing from 2.63 °C in the control run to 1.73 °C in the Sturm run for MAD and from 3.17 to 2.4 °C for RMSE. However, the RMSE values still remain high. This is probably linked to the pronounced warm bias observed over high-altitude areas (e.g. the Central Siberian Plateau, the Verkhoyansk Range, most of eastern Siberia, the northern regions of Baffin Island, and the Brooks Range), which was present in the control run but greatly amplified in the Sturm simulation.

3.2.3 Comparison between the Sturm run and the 295GT dataset

In general, the control run captures the attenuation and delay of the seasonal cycle in soil temperature for period-averaged monthly soil temperatures (Fig. 6) at various depth levels (-20, -80, -160, and -320 cm) reasonably well. However, it consistently exhibits a cold bias of a similar amplitude across all seasons and depths (MAD $= 3.23$ °C and RMSE $= 3.32$ °C for -20 cm; MAD $= 4.35$ °C and RMSE $= 4.35$ °C for -320 cm). The Sturm run effectively minimised the bias gap introduced by the control run, particularly during DJF and within the uppermost soil layers (MAD $= 1.76$ °C and RMSE $= 1.93$ °C for -20 cm). Once the snow had melted out in JJA, the impact of our experiment on snow thermal conductivity decreased, as expected. The slight bias reduction that persists after snowmelt can be attributed to soil temperature memory. In addition, the improvement is less pronounced in deeper layers (MAD $= 2.55$ °C and RMSE $= 2.57$ °C for -320 cm), as the properties of soil increasingly dominate snow insulation properties at depth. Furthermore, there is a notable positive bias of up to 2 °C observed in the top -20 cm soil layer during DJF. On average, the RMSE across the four soil layers decreases from 3.9 °C in the control run to 2.19 °C in the Sturm run.

3.3 Sensitivity analysis to snow density

The sensitivity analysis to snow density shows that the Sturm parameterisation regularly yields lower RMSE values compared to those of Jordan (blue cells in Fig. 7). This improve-
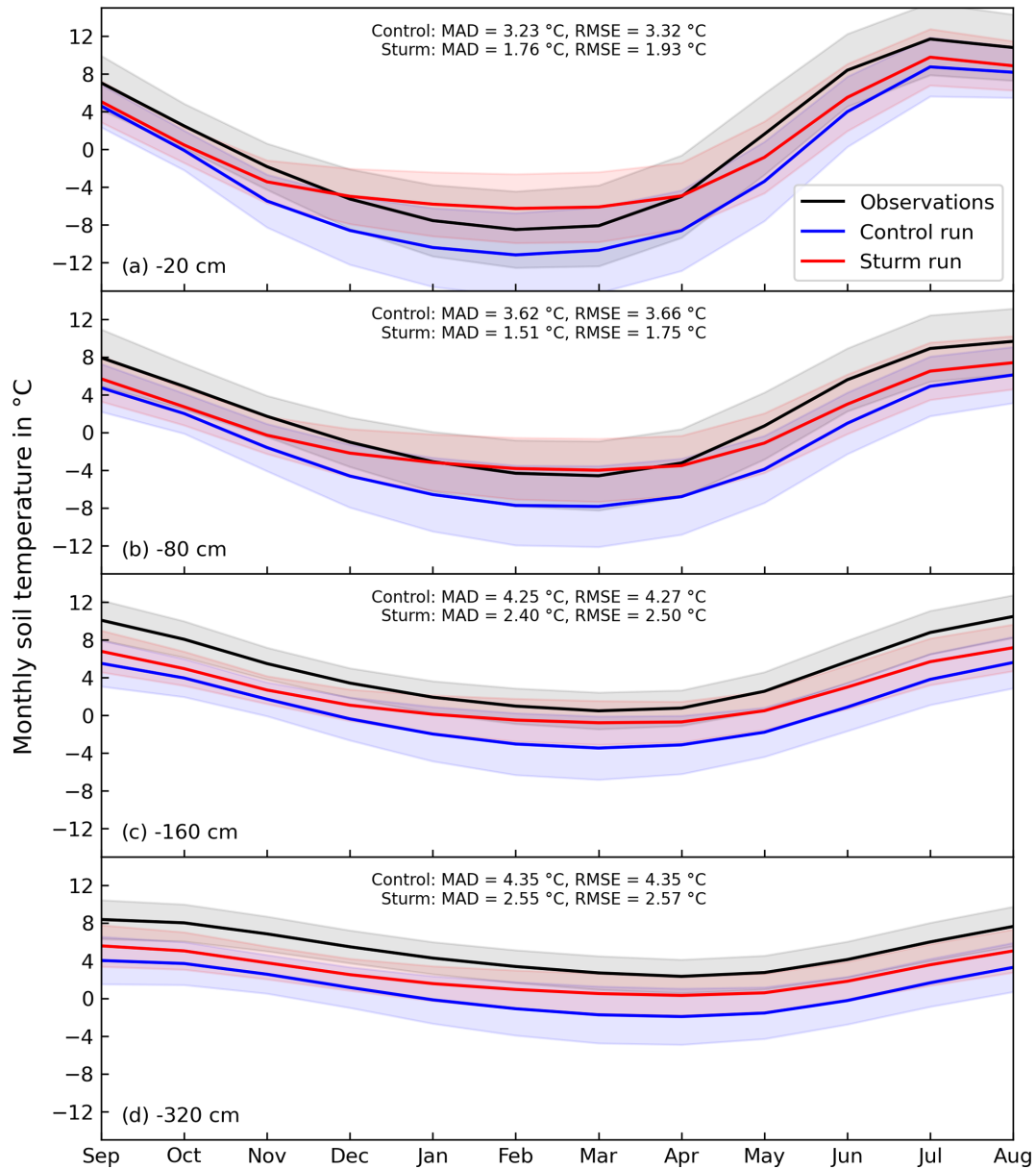
Figure 6. Period-averaged (1980–2021) monthly soil temperature for the observations (black), control run (blue), and Sturm run (red) at 4 different depths: **(a)** −20 cm, **(b)** −80 cm, **(c)** −60 cm, and **(d)** −320 cm. Each of these represents an average of depth ranges as follows: −20 cm is 0–40 cm, −80 cm is 41–120 cm, −160 cm is 121–200 cm, and −320 cm is 201–440 cm. The shaded areas represent the standard deviation over all years. All values and skill scores (MAD, RMSE) come from an average of the 295 stations throughout the full period.

ment is most pronounced during winter months (FMA) in deeper layers of soil. As snow density is reduced, the relative benefit of Sturm over Jordan diminishes, particularly in JFMA months at soil depths of −20 and −80 cm. However, the Sturm parameterisation leads to a lower soil temperature error for most months and depths. During summer months (without snow cover), the winter influence of the Sturm parameterisation continues, simulating a lower temperature error than that of Jordan, particularly in deeper soil layers.

3.4 Permafrost extent

There is strong agreement between the control run and ESA-CCI permafrost extents, with 93 % of the two datasets overlapping, including the discontinuous Arctic permafrost regions (Fig. 8). However, the control run slightly overestimates permafrost extent in the southern regions of Alaska, Canada, and particularly Siberia.

For the Sturm run, the overestimation of permafrost made by the control run has been resolved to the detriment of
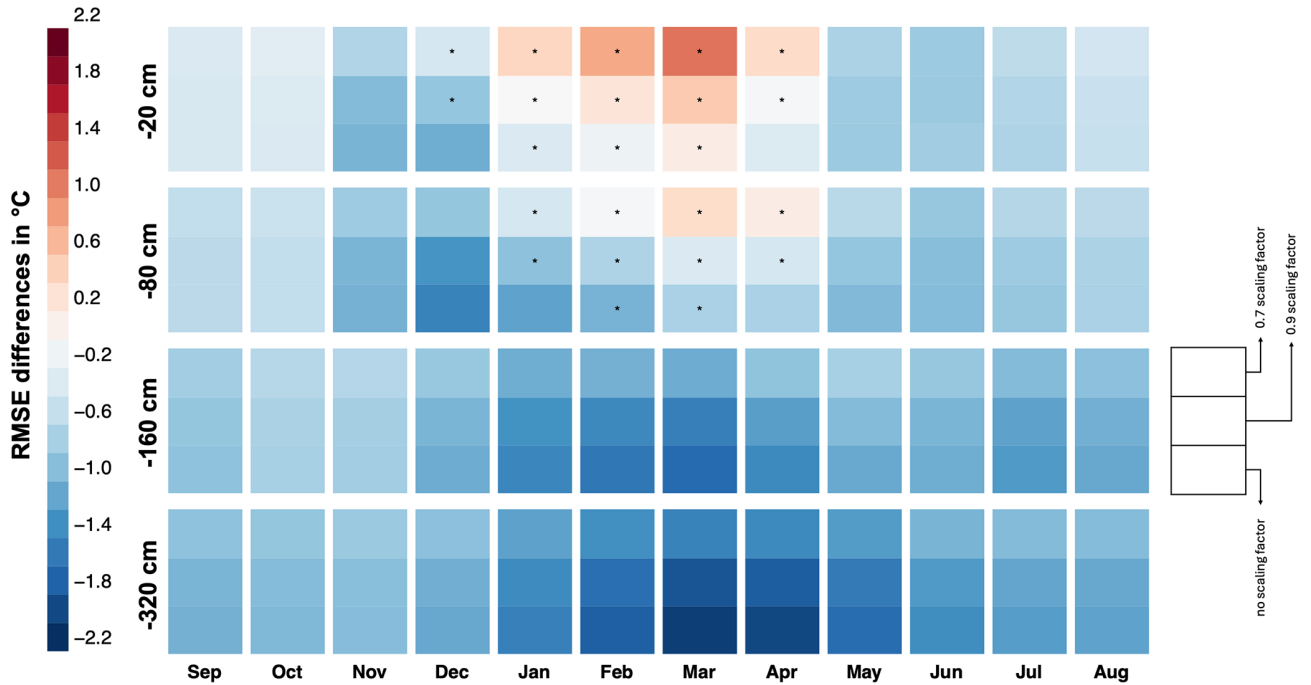
Figure 7. Period-averaged (2006–2010) differences in monthly soil temperature RMSEs (Sturm minus Jordan) across the 295 stations. Each row represents a different depth (−20, −80, −160, and −320 cm), while each column represents the average of a different month. Each cell represents a different adjustment factor: 0.7 (top); 0.9 (middle); and no adjustment factor – default (bottom). Cells with positive MAD values in the Sturm run (overshoots) are marked with an asterisk (*). Darker blue indicates improved RMSE scores in Sturm relative to Jordan.
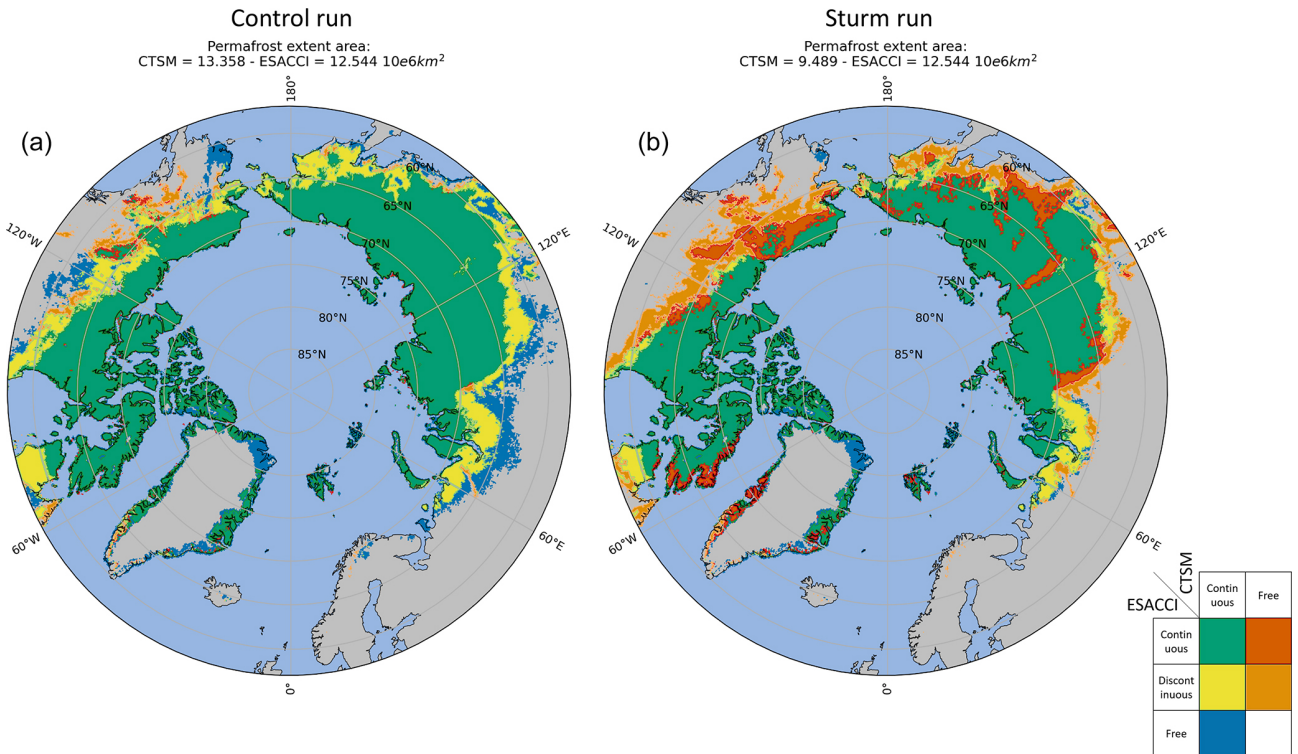
Figure 8. The permafrost extent area mask difference between CTSM and ESA-CCI for the control run (**a**) and the Sturm run (**b**). ESA-CCI data are aggregated on the CTSM grid using a conservative second-order regridding method.
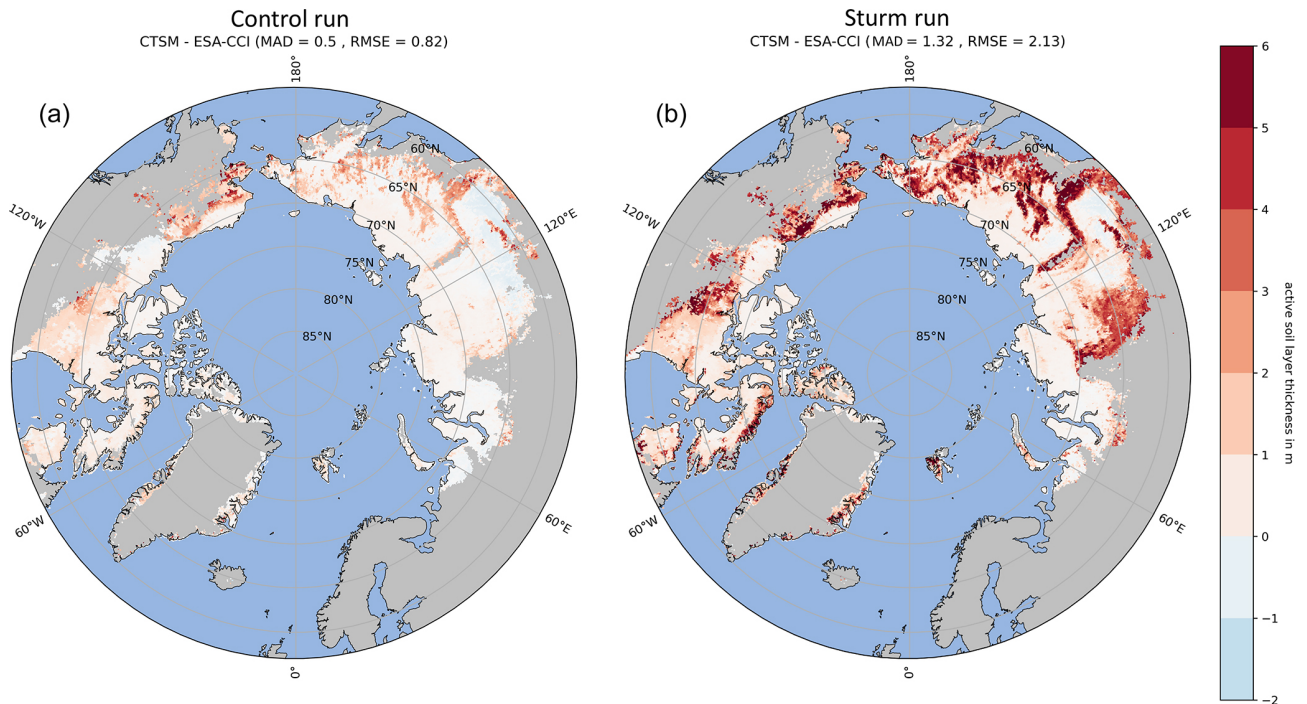
Figure 9. Active-layer thickness difference between CTSM and ESA-CCI (in m) for the control run **(a)** and the Sturm run **(b)**. Darker red indicates that CTSM ALT is deeper than ESA-CCI. ESA-CCI data are aggregated on the CTSM grid using a conservative second-order regridding method. Only regions considered permafrost in the Sturm simulation are shown to facilitate comparison between the two simulations.

mountainous regions (in red) that have been reclassified as non-permafrost (Fig. 8). In addition, the Sturm run shows a marked loss of discontinuous permafrost (in orange). In total, the Sturm run simulates a permafrost extent area equal to $9.489 \times 10^6 \, \text{km}^2$, a strong decrease compared to the control run ($13.358 \times 10^6 \, \text{km}^2$) and ESA-CCI ($12.544 \times 10^6 \, \text{km}^2$) values.

To supplement our analysis with ESA-CCI permafrost extent products, we compare the results of the control and Sturm runs to the International Permafrost Association (IPA) map (Brown et al., 2002) in Fig. A3.

3.5 Active-layer thickness (ALT)

Differences between the CLM5.0 and ESA-CCI ALT products indicate a noticeable positive bias increase (Fig. 9) that varies across regions. While minor biases are observed over tundra areas, biases are significantly amplified over mountainous regions and in the southern Siberian regions with deep active layers. MAD and RMSE scores increase from 0.5 to 1.32 m and from 0.82 to 2.13 m, respectively. Note that we calculated these statistics only within regions identified as permafrost in the Sturm simulation to ensure a direct comparison of identical areas. This approach means that we excluded large regions classified as non-permafrost in the Sturm run from our analysis.

4 Discussion

4.1 Snow insulation

Earlier findings (Wang et al., 2016; Slater et al., 2017) show that there is a logarithmic relationship between the winter offset and snow depth, reaching an asymptote at a snow depth of approximately 25 cm according to in situ observations. In Fig. 3, only the Sturm run accurately represents this logarithmic relationship in cold-temperature regimes. The control run exhibits a trend closer to a linear relationship, often resulting in an underestimation of snow insulation, which is consistent with findings from other modelling groups (Wang et al., 2016; Slater et al., 2017; Guimberteau et al., 2018; Burke et al., 2020; Pongracz et al., 2021). Interestingly, CESM (using CLM5.0) shows a degradation in the representation of that relationship compared to its previous version using CLM4.5 (Burke et al., 2020). We hypothesise that the underestimation of snowpack density by CLM4.5 (Lawrence et al., 2019) combined with the high-thermal-conductivity scheme from Jordan (1991) artificially resulted in adequate snow insulation represented by the model over Arctic tundra regions. The introduction of the new fresh-snow-density function by van Kampenhout et al. (2017) in CLM5.0 may have had unintended consequences, making the bulk snow density too high in Arctic tundra regions, where specific tundra snowpack features like depth hoar are not rep-

resented by the model (van Kampenhout et al., 2017). As the snow thermal conductivity scheme remained unchanged from CLM4.5 to CLM5.0, higher snow densities mean that heat energy from the soil can be lost to the atmosphere more efficiently, which may explain the notable cold bias observed in CLM5.0.

The spatial distribution of the winter offset in the Sturm run better aligns with previous findings (Wang et al., 2016) compared to the control run, despite the minimal difference in effective snow depth between the two runs (below $\pm 5\%$ in most regions; see Fig. A4). This supports our hypothesis that the snow insulation in the Sturm simulation is considerably increased and is generally more representative of tundra snowpacks.

4.2 Soil temperature

The magnitude of the cold bias observed in the control run is similar to what other modelling groups have shown (Dankers et al., 2011; Burke et al., 2013; Wang et al., 2013; Ekici et al., 2014; Barrere et al., 2017; Guimberteau et al., 2018; Pongracz et al., 2021), especially over colder regions, and tends to be more pronounced in deeper layers. On the other hand, some evaluations of LSMs have reported the absence of such a bias (Chadburn et al., 2015; Decharme et al., 2016; Chadburn et al., 2017). However, these studies rely on sparse in situ measurements (often with an absence of observations in high-latitude regions) that may not fully represent the entire pan-Arctic domain. Other studies evaluating coupled LSM–Snowpack models have shown very good performance in soil temperature representation in the pan-Arctic region (Barrere et al., 2017; Royer et al., 2021), underscoring the importance of accurate snow physics, albeit at a higher computational cost. Our results reveal a bias amplitude consistent across all seasons and depths, reflecting findings from prior research (Burke et al., 2013; Paquin and Sushama, 2015). This contrasts with several model studies (Dankers et al., 2011; Wang et al., 2013; Barrere et al., 2017; Guimberteau et al., 2018; Oogathoo et al., 2022) that show larger biases in winter compared to summer. Interestingly, our findings align with similar trends observed in the study by Herrington et al. (2024), which examined the performance of reanalysis soil temperature data across the pan-Arctic domain and noted a prevalent cold bias.

The results of the Sturm run are consistent with a comparable experiment on snow thermal conductivity conducted by Paquin and Sushama (2015), showing a decrease in wintertime soil temperature bias and a diminishing improvement with depth. However, our results show closer alignment with the observations. Conversely, the model study by Oogathoo et al. (2022) using the Sturm et al. (1997) equation indicates an underestimation of soil temperature in winter, although their model uses a basic snowpack model with a single layer.

The persistent cold bias in simulated soil temperature in deeper layers may be attributed to several missing snow processes, including more realistic snow metamorphism (Decharme et al., 2016) or upward water vapour mass transfers within the snowpack (Domine et al., 2019). Recent studies have explored these missing processes (Brondex et al., 2023; Fourteau et al., 2024). Additionally, soil processes such as the inclusion of excess ground ice (Lee et al., 2014; Burke et al., 2020), an improved phase-change scheme (Yang et al., 2018; Tao et al., 2021), and the development of adapted frozen-soil thermal conductivity models (He et al., 2021) offer greater potential to improve the soil temperature accuracy in summer and at depth.

In general, the model skill scores perform better against grid-based-observation datasets rather than against in situ observations (RMSE = 3.17–3.24 °C against ESA-CCI, RMSE = 3.32–4.35 °C against 295GT for the control run). The divergence between model outputs and in situ observations is often attributed to the inherent scale differences. While the model operates at a coarse resolution ($12\,km^2$), observations are site-specific. Comparing point observations to model grid points covering a wide area can lead to inaccuracies because individual observations may not fully represent the characteristics of the model grid-point-covered area (Dankers et al., 2011; Park et al., 2015). Scale disparities commonly stem from variations in elevation, climate, soil composition, and landscape characteristics, resulting in considerable diversity in soil thermal and hydraulic properties and, consequently, in soil temperature patterns.

Large positive-soil-temperature biases of up to 8 °C are particularly noticeable over high-altitude regions in our ESA-CCI evaluation. This discrepancy arises in part from variations in atmospheric forcing resolution between CLM5.0 ($12\,km^2$) and ESA-CCI ($1\,km^2$); lower-resolution models smooth out complex mountain terrain features into larger grid cells, leading to an inadequate representation of temperature in mountain environments (El-Samra et al., 2018). Secondly, the parameterisation of the Sturm scheme assumes the presence of basal depth hoar and overlying wind slab, potentially leading to inaccurate representation of the thermal conductivity of the basal and mid-depth snow types typically found in mountainous regions (Sturm et al., 1997). The application of different empirical snow thermal conductivity schemes based on snow types (e.g. tundra or alpine) may address this challenge. However, identifying both the meteorological and land surface conditions needed for accurate application of such schemes in a global model like CLM would be challenging.

4.3 Sensitivity analysis to snow density

As previously stated, studies show that state-of-the-art LSMs and snowpack models, including CLM5.0, have vertical density profiles often exhibiting significant discrepancies from observed snow density, in both the top wind slab and bottom depth hoar layers of the snowpack. Such discrepancies lead to over-densification in the simulated tundra snowpack.

The misrepresentation arises because the scheme does not account for the temperature-gradient metamorphism, a process that creates low-density depth hoar layers in tundra snowpacks (Dutch et al., 2022). Without this mechanism, the simulated snow can only increase in density with age, leading to bulk densities that exceed observed values in these regions. Incorporating temperature-gradient metamorphism in future model developments would likely result in lower simulated snow densities, improving agreement with field observations (Brondex et al., 2023).

Our sensitivity analysis shows that the RMSE reductions achieved by the Sturm parameterisation remain robust, even if future improvements are made to tundra snow densification processes that result in lower bulk densities. This improvement is most pronounced in deeper layers during winter months (FMA), when the cold wave penetrates deeply, emphasising the relevance for permafrost modelling. This suggests that the improved performance of the Sturm model over that of Jordan does not rely on unrealistically high bulk snow density values. However, the increase in RMSE caused by the overestimation of soil temperatures in upper layers during winter months is amplified when snow density is reduced. While this highlights a limitation of the Sturm scheme in certain scenarios, the overall benefits for permafrost modelling outweigh this drawback, particularly in the context of deeper soil layers where winter thermal dynamics are critical.

4.4 Permafrost extent

The comparison between the ESA-CCI permafrost data and our model results involves inherent uncertainties due to differences in spatial resolution. Our land model's grid cells are approximately 100 times larger than those of the ESA-CCI product, leading to blurred boundaries when aggregating the data. Although the ESA-CCI data itself has uncertainties, with most grid cells having uncertainties below 50 %, these are unlikely to outweigh the uncertainties introduced by the resolution mismatch.

Several other modelling groups observe an overestimation of the permafrost extent similar to the control run, as indicated by the Coupled Model Intercomparison Project version 6 (CMIP6) on permafrost physics (Burke et al., 2020), although not all models show this behaviour. While the Sturm run provides some mitigation of this pattern, some continuous and discontinuous permafrost areas over mountains and southern Alaska, Canada, and Siberia are lost. The issue may arise from the presence of warm permafrost at the southern edge where ground temperatures approach 0 °C and the soil moisture content is high. Over those regions, the accuracy of the ESA-CCI products is affected because latent heat effects slow down potential thaw, which increases the disequilibrium between atmospheric and ground temperatures (Obu et al., 2019). The area simulated in this study is similar to that modelled by Paquin and Sushama (2015) in their Sturm

experiment; however, their high-altitude regions remain classified as permafrost.

4.5 Active layer

In general, both CLM5.0 configurations show a tendency to overestimate maximum thaw depth, a trend exacerbated in the Sturm run in high-altitude and southern regions. This discrepancy has been observed in many other LSM studies (Dankers et al., 2011; Ekici et al., 2014; Chadburn et al., 2015; Paquin and Sushama, 2015; Guimberteau et al., 2018; Burke et al., 2020; Tao et al., 2024). Using a knowledge-based hierarchical optimisation strategy on a series of parameters (precipitation-phase partitioning, snow compaction, and snow thermal conductivity) and input data (climate forcings and SOC density profile), Tao et al. (2024) effectively enhanced ALT results across more than 100 pan-Arctic sites in their LSM. While their methodology shows promise, its implementation across various model set-ups and models will require thoughtful adaptation and adjustments.

CLM5.0 performs better in high-latitude tundra regions compared to other modelling groups, which often display more pronounced regional biases. Notably, our study is the first to evaluate an LSM's ALT against a grid-based observation product, whereas most other studies to date compare their ALT results to in situ station data, e.g. CALM in Shiklomanov et al. (2012). The discrepancy observed in southern regions may also be attributed to challenges faced by ESA-CCI data methods, such as probing and ground-penetrating radar, in accurately measuring ALT in regions with deeper active layers (Liu et al., 2024). Our findings highlight the critical need for diverse, regionally tailored observational datasets to refine model performance and better capture the complexities of permafrost dynamics.

5 Conclusions

With the growing need to assess the substantial impact of permafrost–carbon feedbacks on global climate, it is increasingly important for land surface models (LSMs) to accurately represent ground temperature in permafrost tundra regions. Snow plays a critical role over these regions, providing thermal insulation during winter, which has substantial implications for heat exchange between the atmosphere and the soil. However, Earth system models (ESMs) often lack sufficient detail regarding the spatial and temporal variability in snow insulation, among other factors.

Building upon a site experiment at Trail Valley Creek (Dutch et al., 2022), this paper applies the Sturm et al. (1997) relationship between snow thermal conductivity and density to the entire pan-Arctic domain, as it is better suited to the snow density profile found over Arctic tundra permafrost regions. Our aim was to study the impact of this scheme on simulated soil temperatures and permafrost dynamics,

thereby improving the model's performance in reproducing snow physics over Arctic tundra regions.

The integration of the Sturm et al. (1997) snow thermal conductivity scheme within CLM5.0 resulted in a reduction in cold biases and a closer alignment of model outputs with observational datasets (against remote sensing data, RMSE decreases from 3.17 to 2.4 °C; against in situ data, RMSE decreases from 3.9 to 2.19 °C). Our sensitivity analysis of snow density further validates the robustness of the Sturm parameterisation, demonstrating that its improvements persist even when accounting for potentially lower bulk snow densities in tundra environments. Furthermore, the Sturm experiment effectively addresses the overestimation of permafrost observed in the control run in southern Siberia and Canada. However, large areas over discontinuous permafrost and mountainous regions were reclassified as non-permafrost. Altogether, the Sturm run simulates a permafrost extent area of 9.489×10^6 km^2, a significant decrease compared to both the control run (13.358×10^6 km^2) and the ESA-CCI (12.544×10^6 km^2) values. In addition, we observed a notable increase in the ALT bias, primarily in mountainous areas. We attribute the bias observed over high-altitude regions to two possible factors: (1) differences in the resolution of the atmospheric forcing data used in ESA-CCI and CLM5.0 and (2) potential lack of suitability in the newly implemented snow scheme in mountainous regions.

While the Sturm parameterisation offers a substantial improvement, addressing cold biases and enhancing the simulation of snow insulation in Arctic regions, it is not a panacea. Future advancements in the CLM snow scheme, particularly in the representation of snow stratigraphy and processes such as water vapour transport, will be necessary to further refine these simulations and improve model accuracy. The value of improved tundra snow thermal representation in an LSM needs testing within a fully coupled ESM to understand how consequent changes in simulated soil temperatures impact vegetation (Jin et al., 2021); river flows (Rawlins and Karmalkar, 2024); permafrost-thaw-related CO_2 emissions (Dutch et al., 2023); and consequently, climate feedbacks (Schädel et al., 2024). Overall, our findings underscore the importance of refining snow-related processes in LSMs to enhance broader understanding of permafrost dynamics in the context of climate change.

Appendix A: Additional figures

A1   Snow thermal conductivity schemes

Figure A1 provides a comparison of five different schemes for effective thermal conductivity (K_{eff}) across a range of snow densities from 0 to 700 kg m^{-3}. The Sturm scheme demonstrates lower K_{eff} values in comparison to the other schemes, particularly within the range of snow densities en-
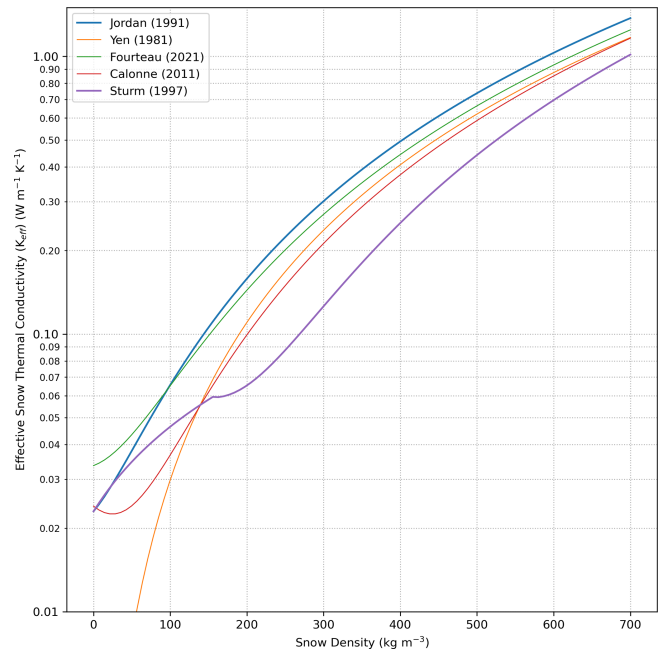
Figure A1. Comparison of five schemes for K_{eff} from 0 to 700 kg m^{-3} for snow density. Note that the y axis is logarithmic.

countered in permafrost regions that typically fall between 200 to 300 kg m^{-3}.

A2   Bulk snow density

Figure A2 represents the spatial and statistical distribution of bulk snow density for the control run in our domain. The bulk snow density is calculated using the snow water equivalent (SWE) (in m) and snow depth (in m) through the following equation:

$$\rho_{sno} = \rho_w \frac{SWE}{SD}, \tag{A1}$$

where ρ_w is the density of liquid water (1000 kg m^{-3}). The mean density is 311 kg m^{-3}, with an interquartile range (P25–P75) of 216 to 380 kg m^{-3}. The histogram reveals a multimodal distribution, indicative of different snowpack types (e.g. tundra, maritime, alpine).

A3   Comparison against the permafrost extent Brown map

The IPA categorises permafrost into four distinct classes based on its areal coverage: continuous permafrost (90 %–100 %), discontinuous permafrost (50 %–90 %), sporadic permafrost (10 %–50 %), and isolated permafrost (less than 10 %). Similar to our comparison with ESA-CCI, we compare the continuous and discontinuous IPA categories and assumed areas below 50 % coverage to be permafrost-free to align with our binary definition of permafrost.
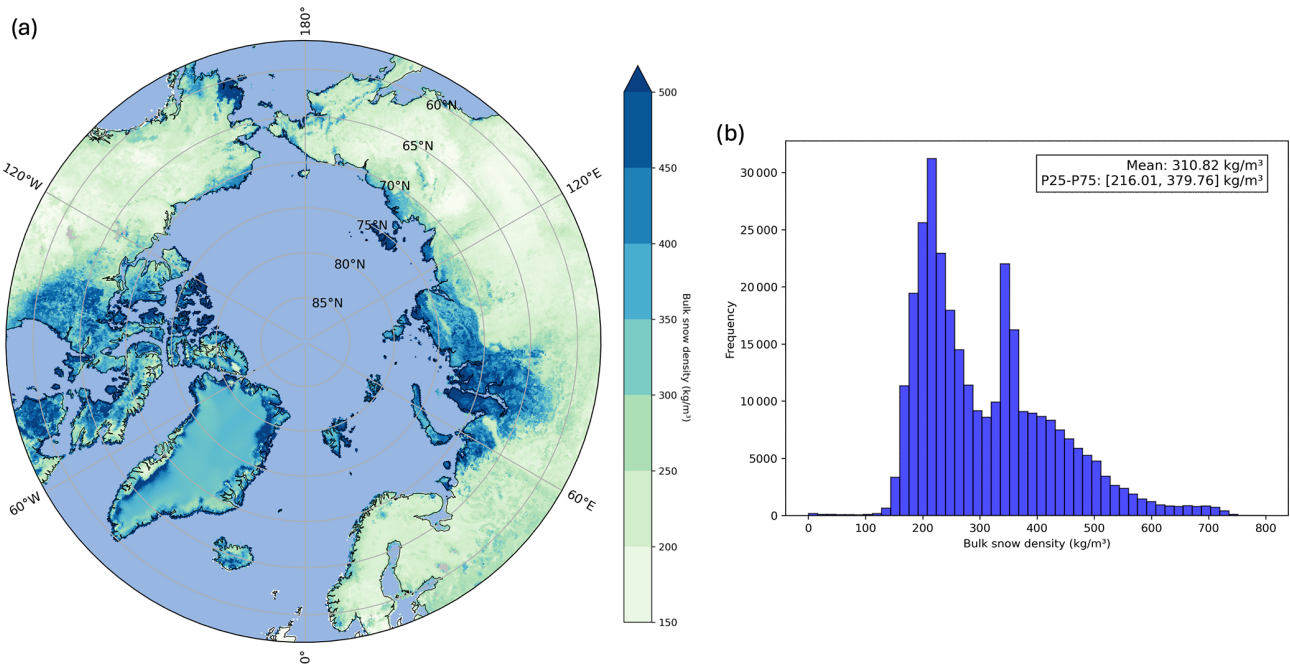
Figure A2. Period-averaged (1980–2021) bulk snow density for **(a)** the control run and **(b)** its corresponding histogram.
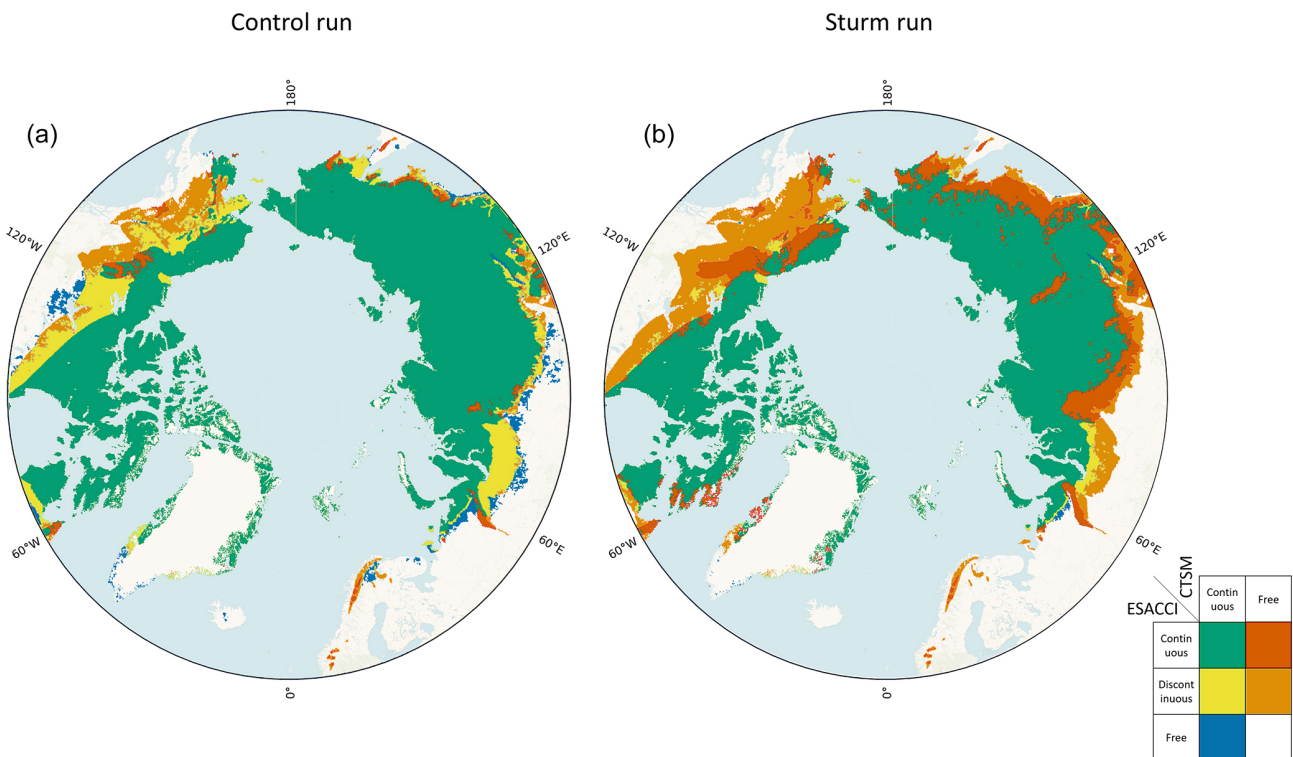
Figure A3. The permafrost extent area difference between the CTSM control and Sturm runs (1981–1999) and the Brown et al. (2002) map.

The permafrost extent estimated in Brown et al. (2002) surpasses that of ESA-CCI data across southern Siberia, resulting in a nearly negligible overestimation in the control run over this area (Fig. A3). However, the model fails to capture a substantial portion of discontinuous permafrost over southern Alaska.

As expected, this discrepancy leads to a more pronounced underestimation of permafrost extent in the Sturm run in many regions, including Alaska, southern Canada, and southern Siberia alongside previously mentioned areas, compared to ESA-CCI products.

It is worth noting that this comparison may be less practical than the comparison with ESA-CCI products. The Brown et al. (2002) data, compiled and digitised in the 1990s from historical records, represent an estimate of permafrost extent during the latter half of the 20th century (Burke et al., 2013). They are compared with model results covering the period of 1981–1999, suggesting a potentially lower permafrost extent than in the latter half of the 20th century.

A4 Effective snow depth in the Sturm and control runs

The effective snow depth characterises the insulation provided by snow during the cold period (Burke et al., 2020). $S_{\text{depth,eff}}$ is a cumulative value where the average snow depth in each month, denoted S_{m} (in m), is adjusted according to its duration:

$$S_{\text{depth,eff}} = \frac{\sum_{m=1}^{M} S_{\text{m}}(M+1-m)}{\sum_{m=1}^{M} m}. \quad (A2)$$

Snow can be present anytime from October ($m = 1$) to March ($m = 6$), with the maximum duration, M, being 6 months. This weighting approach favours early snowfall over late snowfall, as it contributes more to the overall insulating effect. When the effective snow depth, $S_{\text{depth,eff}}$, surpasses 0.25 m, the insulating capacity of the snow remains relatively constant (Burke et al., 2020), and seasons with earlier snowfall typically exhibit higher $S_{\text{depth,eff}}$ than seasons with later snowfall.

Figure A4 shows the period-averaged percentage change in effective snow depth between the control and Sturm simulations, highlighting the fact that there are few regions with percent changes higher than +5 or lower than −5. Percentage change is calculated as

$$\text{Percentage change} = \left(\frac{S_{\text{depth,eff,sturm}} - S_{\text{depth,eff,control}}}{S_{\text{depth,eff,control}}} \right) \times 100 \quad . \quad (A3)$$
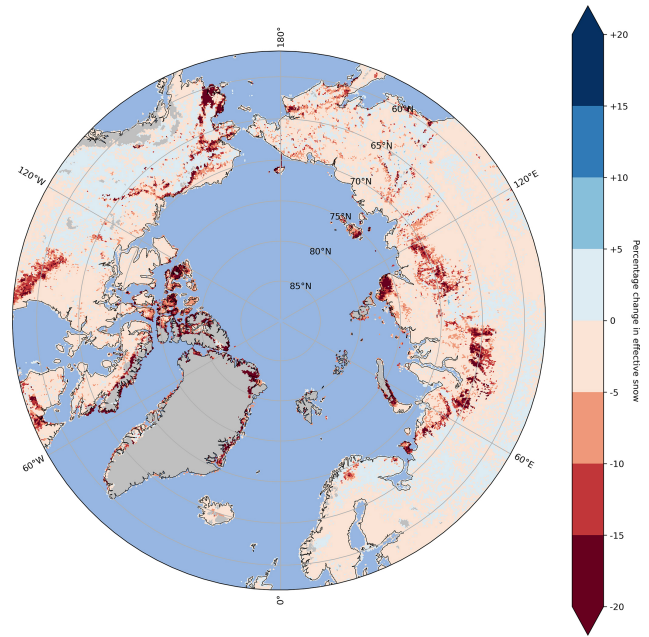
Figure A4. Percent change in effective snow (1980–2021 period average) between the control and Sturm runs. Darker red indicates that the Sturm run effective snow is lower than that of the control run. The grey mask represents glaciers.

References

Adams, E. E. and Sato, A.: Model for effective thermal conductivity of a dry snow cover composed of uniform ice spheres, Ann. Glaciol., 18, 300–304, https://doi.org/10.3189/S026030550001168X, 1993.

Albergel, C., Dutra, E., Munier, S., Calvet, J.-C., Munoz-Sabater, J., de Rosnay, P., and Balsamo, G.: ERA-5 and ERA-Interim driven ISBA land surface model simulations: which one performs better?, Hydrol. Earth Syst. Sci., 22, 3515–3532, https://doi.org/10.5194/hess-22-3515-2018, 2018.

Anderson, E. A.: A point energy and mass balance model of a snow cover, NOAA technical report NWS, 19, NOAA, Washington, DC, 150 pp., https://www.proquest.com/docview/302818861?pq-origsite=gscholar&fromopenview=true (last access: 8 April 2025), 1976.

Barrere, M., Domine, F., Decharme, B., Morin, S., Vionnet, V., and Lafaysse, M.: Evaluating the performance of coupled snow–soil models in SURFEXv8 to simulate the permafrost thermal regime at a high Arctic site, Geosci. Model Dev., 10, 3461–3479, https://doi.org/10.5194/gmd-10-3461-2017, 2017.

Bartelt, P. and Lehning, M.: A physical SNOWPACK model for the Swiss avalanche warning, Cold Reg. Sci. Technol., 35, 123–145, https://doi.org/10.1016/S0165-232X(02)00074-5, 2002.

Best, M. J., Pryor, M., Clark, D. B., Rooney, G. G., Essery, R. L. H., Ménard, C. B., Edwards, J. M., Hendry, M. A., Porson, A., Gedney, N., Mercado, L. M., Sitch, S., Blyth, E., Boucher, O., Cox, P. M., Grimmond, C. S. B., and Harding, R. J.: The Joint UK Land Environment Simulator (JULES), model description – Part 1: Energy and water fluxes, Geosci. Model Dev., 4, 677–699, https://doi.org/10.5194/gmd-4-677-2011, 2011.

Birch, L., Schwalm, C. R., Natali, S., Lombardozzi, D., Keppel-Aleks, G., Watts, J., Lin, X., Zona, D., Oechel, W., Sachs, T., Black, T. A., and Rogers, B. M.: Addressing biases in Arctic–boreal carbon cycling in the Community Land Model Version 5, Geosci. Model Dev., 14, 3361–3382, https://doi.org/10.5194/gmd-14-3361-2021, 2021.

Boone, A., Samuelsson, P., Gollvik, S., Napoly, A., Jarlan, L., Brun, E., and Decharme, B.: The interactions between soil–biosphere–atmosphere land surface model with a multi-energy balance (ISBA-MEB) option in SURFEXv8 – Part 1: Model description, Geosci. Model Dev., 10, 843–872, https://doi.org/10.5194/gmd-10-843-2017, 2017.

Brondex, J., Fourteau, K., Dumont, M., Hagenmuller, P., Calonne, N., Tuzet, F., and Löwe, H.: A finite-element framework to explore the numerical solution of the coupled problem of heat conduction, water vapor diffusion, and settlement in dry snow (IvoriFEM v0.1.0), Geosci. Model Dev., 16, 7075–7106, https://doi.org/10.5194/gmd-16-7075-2023, 2023.

Brown, J., Heginbottom, J., Ferrians, O., and Melnikov, E.: Circum-Arctic Map of Permafrost and Ground-Ice Conditions, Version 2, NSIDC [data set], https://doi.org/10.7265/SKBG-KF16, 2002.

Burke, E. J., Dankers, R., Jones, C. D., and Wiltshire, A. J.: A retrospective analysis of pan Arctic permafrost using the JULES land surface model, Clim. Dynam., 41, 1025–1038, https://doi.org/10.1007/s00382-012-1648-x, 2013.

Burke, E. J., Zhang, Y., and Krinner, G.: Evaluating permafrost physics in the Coupled Model Intercomparison Project 6 (CMIP6) models and their sensitivity to climate change, The Cryosphere, 14, 3155–3174, https://doi.org/10.5194/tc-14-3155-2020, 2020.

Calonne, N., Flin, F., Morin, S., Lesaffre, B., Du Roscoat, S. R., and Geindreau, C.: Numerical and experimental investigations of the effective thermal conductivity of snow, Geophys. Res. Lett., 38, L23501, https://doi.org/10.1029/2011GL049234, 2011.

Chadburn, S. E., Burke, E. J., Essery, R. L. H., Boike, J., Langer, M., Heikenfeld, M., Cox, P. M., and Friedlingstein, P.: Impact of model developments on present and future simulations of permafrost in a global land-surface model, The Cryosphere, 9, 1505–1521, https://doi.org/10.5194/tc-9-1505-2015, 2015.

Chadburn, S. E., Krinner, G., Porada, P., Bartsch, A., Beer, C., Belelli Marchesini, L., Boike, J., Ekici, A., Elberling, B., Friborg, T., Hugelius, G., Johansson, M., Kuhry, P., Kutzbach, L., Langer, M., Lund, M., Parmentier, F.-J. W., Peng, S., Van Huissteden, K., Wang, T., Westermann, S., Zhu, D., and Burke, E. J.: Carbon stocks and fluxes in the high latitudes: using site-level data to evaluate Earth system models, Biogeosciences, 14, 5143–5169, https://doi.org/10.5194/bg-14-5143-2017, 2017.

Cheng, Y., Musselman, K. N., Swenson, S., Lawrence, D., Hamman, J., Dagon, K., Kennedy, D., and Newman, A. J.: Moving Land Models Toward More Actionable Science: A Novel Application of the Community Terrestrial Systems Model Across Alaska and the Yukon River Basin, Water Resour. Res., 59, e2022WR032204, https://doi.org/10.1029/2022WR032204, 2023.

CTSM Development Team: AdrienDams/CTSM: sturm-paper (v1.0.0), Zenodo [code], https://doi.org/10.5281/zenodo.15174742, 2025.

Damseaux, A.: On Using an Alternative Snow Thermal Conductivity Scheme in CLM5 over the Arctic, DOKU at DKRZ [data set], https://hdl.handle.net/21.14106/a519e929139bdadd0b4a1c9d691799fbba48b22f (last access: 8 April 2025), 2023.

Damseaux, A.: AdrienDams/cegio: sturm-paper (1.0.0), Zenodo [code], https://doi.org/10.5281/zenodo.15174670, 2025.

Dankers, R., Burke, E. J., and Price, J.: Simulation of permafrost and seasonal thaw depth in the JULES land surface scheme, The Cryosphere, 5, 773–790, https://doi.org/10.5194/tc-5-773-2011, 2011.

Decharme, B., Brun, E., Boone, A., Delire, C., Le Moigne, P., and Morin, S.: Impacts of snow and organic soils parameterization on northern Eurasian soil temperature profiles simulated by the ISBA land surface model, The Cryosphere, 10, 853–877, https://doi.org/10.5194/tc-10-853-2016, 2016.

Domine, F., Barrere, M., and Sarrazin, D.: Seasonal evolution of the effective thermal conductivity of the snow and the soil in high Arctic herb tundra at Bylot Island, Canada, The Cryosphere, 10, 2573–2588, https://doi.org/10.5194/tc-10-2573-2016, 2016.

Domine, F., Belke-Brea, M., Sarrazin, D., Arnaud, L., Barrere, M., and Poirier, M.: Soil moisture, wind speed and depth hoar formation in the Arctic snowpack, J. Glaciol., 64, 990–1002, https://doi.org/10.1017/jog.2018.89, 2018.

Domine, F., Picard, G., Morin, S., Barrere, M., Madore, J.-B., and Langlois, A.: Major Issues in Simulating Some Arctic Snowpack Properties Using Current Detailed Snow Physics Models: Consequences for the Thermal Regime and Water Budget of Permafrost, J. Adv. Model. Earth Sy., 11, 34–44, https://doi.org/10.1029/2018MS001445, 2019.

Dutch, V. R., Rutter, N., Wake, L., Sandells, M., Derksen, C., Walker, B., Hould Gosselin, G., Sonnentag, O., Essery, R., Kelly, R., Marsh, P., King, J., and Boike, J.: Impact of measured and simulated tundra snowpack properties on heat transfer, The Cryosphere, 16, 4201–4222, https://doi.org/10.5194/tc-16-4201-2022, 2022.

Dutch, V. R., Rutter, N., Wake, L., Sonnentag, O., Hould Gosselin, G., Sandells, M., Derksen, C., Walker, B., Meyer, G., Essery, R., Kelly, R., Marsh, P., Boike, J., and Detto, M.: Simulating net ecosystem exchange under seasonal snow cover at an Arctic tundra site, EGUsphere [preprint], https://doi.org/10.5194/egusphere-2023-772, 2023.

Ekici, A., Beer, C., Hagemann, S., Boike, J., Langer, M., and Hauck, C.: Simulating high-latitude permafrost regions by the JSBACH terrestrial ecosystem model, Geosci. Model Dev., 7, 631–647, https://doi.org/10.5194/gmd-7-631-2014, 2014.

El-Samra, R., Bou-Zeid, E., and El-Fadel, M.: What model resolution is required in climatological downscaling over complex terrain?, Atmos. Res., 203, 68–82, https://doi.org/10.1016/j.atmosres.2017.11.030, 2018.

Fourteau, K., Domine, F., and Hagenmuller, P.: Impact of water vapor diffusion and latent heat on the effective thermal conductivity of snow, The Cryosphere, 15, 2739–2755, https://doi.org/10.5194/tc-15-2739-2021, 2021.

Fourteau, K., Brondex, J., Brun, F., and Dumont, M.: A novel numerical implementation for the surface energy budget of melting snowpacks and glaciers, Geosci. Model Dev., 17, 1903–1929, https://doi.org/10.5194/gmd-17-1903-2024, 2024.

Golaz, J., Caldwell, P. M., Van Roekel, L. P., Petersen, M. R., Tang, Q., Wolfe, J. D., Abeshu, G., Anantharaj, V., Asay-Davis, X. S., Bader, D. C., Baldwin, S. A., Bisht, G., Bogenschutz, P. A., Branstetter, M., Brunke, M. A., Brus, S. R., Burrows, S. M., Cameron-Smith, P. J., Donahue, A. S., Deakin, M., Easter, R. C., Evans, K. J., Feng, Y., Flanner, M., Foucar, J. G., Fyke, J. G., Griffin, B. M., Hannay, C., Harrop, B. E., Hoffman, M. J., Hunke, E. C., Jacob, R. L., Jacobsen, D. W., Jeffery, N., Jones, P. W., Keen, N. D., Klein, S. A., Larson, V. E., Leung, L. R., Li, H., Lin, W., Lipscomb, W. H., Ma, P., Mahajan, S., Maltrud, M. E., Mametjanov, A., McClean, J. L., McCoy, R. B., Neale, R. B., Price, S. F., Qian, Y., Rasch, P. J., Reeves Eyre, J. E. J., Riley, W. J., Ringler, T. D., Roberts, A. F., Roesler, E. L., Salinger, A. G., Shaheen, Z., Shi, X., Singh, B., Tang, J., Taylor, M. A., Thornton, P. E., Turner, A. K., Veneziani, M., Wan, H., Wang, H., Wang, S., Williams, D. N., Wolfram, P. J., Worley, P. H., Xie, S., Yang, Y., Yoon, J., Zelinka, M. D., Zender, C. S., Zeng, X., Zhang, C., Zhang, K., Zhang, Y., Zheng, X., Zhou, T., and Zhu, Q.: The DOE E3SM Coupled Model Version 1: Overview and Evaluation at Standard Resolution, J. Adv. Model. Earth Sy., 11, 2089–2129, https://doi.org/10.1029/2018MS001603, 2019.

Gouttevin, I., Langer, M., Löwe, H., Boike, J., Proksch, M., and Schneebeli, M.: Observation and modelling of snow at a polygonal tundra permafrost site: spatial variability and thermal implications, The Cryosphere, 12, 3693–3717, https://doi.org/10.5194/tc-12-3693-2018, 2018.

Guimberteau, M., Zhu, D., Maignan, F., Huang, Y., Yue, C., Dantec-Nédélec, S., Ottlé, C., Jornet-Puig, A., Bastos, A., Laurent, P., Goll, D., Bowring, S., Chang, J., Guenet, B., Tifafi, M., Peng, S., Krinner, G., Ducharne, A., Wang, F., Wang, T., Wang, X., Wang, Y., Yin, Z., Lauerwald, R., Joetzjer, E., Qiu, C., Kim, H., and Ciais, P.: ORCHIDEE-MICT (v8.4.1), a land surface model for the high latitudes: model description and validation, Geosci. Model Dev., 11, 121–163, https://doi.org/10.5194/gmd-11-121-2018, 2018.

He, H., Flerchinger, G. N., Kojima, Y., Dyck, M., and Lv, J.: A review and evaluation of 39 thermal conductivity models for frozen soils, Geoderma, 382, 114694, https://doi.org/10.1016/j.geoderma.2020.114694, 2021.

Heim, B., Lisovski, S., Wieczorek, M., Pellet, C., Delaloye, R., Bartsch, A., Jakober, D., Pointner, G., Strozzi, T., and Seifert, F. M.: D4.1 Product Validation and Intercomparison Report (PVIR), European Space Agency (ESA), https://climate.esa.int/media/documents/CCI_PERMA_PVIR_v3.0_20210930.pdf (last access: 8 April 2025), 2021.

Herrington, T. C., Fletcher, C. G., and Kropp, H.: Validation of pan-Arctic soil temperatures in modern reanalysis and data assimilation systems, The Cryosphere, 18, 1835–1861, https://doi.org/10.5194/tc-18-1835-2024, 2024.

Hersbach, H., Bell, B., Berrisford, P., Hirahara, S., Horányi, A., Muñoz-Sabater, J., Nicolas, J., Peubey, C., Radu, R., Schepers, D., Simmons, A., Soci, C., Abdalla, S., Abellan, X., Balsamo, G., Bechtold, P., Biavati, G., Bidlot, J., Bonavita, M., Chiara, G., Dahlgren, P., Dee, D., Diamantakis, M., Dragani, R., Flemming, J., Forbes, R., Fuentes, M., Geer, A., Haimberger, L., Healy, S., Hogan, R. J., Hólm, E., Janisková, M., Keeley, S., Laloyaux, P., Lopez, P., Lupu, C., Radnoti, G., Rosnay, P., Rozum, I., Vamborg, F., Villaume, S., and Thépaut, J.: The ERA5

global reanalysis, Q. J. Roy. Meteor. Soc., 146, 1999–2049, https://doi.org/10.1002/qj.3803, 2020.

Hu, G., Zhao, L., Li, R., Park, H., Wu, X., Su, Y., Guggenberger, G., Wu, T., Zou, D., Zhu, X., Zhang, W., Wu, Y., and Hao, J.: Water and heat coupling processes and its simulation in frozen soils: Current status and future research directions, CATENA, 222, 106844, https://doi.org/10.1016/j.catena.2022.106844, 2023.

Hugelius, G., Tarnocai, C., Broll, G., Canadell, J. G., Kuhry, P., and Swanson, D. K.: The Northern Circumpolar Soil Carbon Database: spatially distributed datasets of soil coverage and soil carbon storage in the northern permafrost regions, Earth Syst. Sci. Data, 5, 3–13, https://doi.org/10.5194/essd-5-3-2013, 2013.

Jin, X.-Y., Jin, H.-J., Iwahana, G., Marchenko, S. S., Luo, D.-L., Li, X.-Y., and Liang, S.-H.: Impacts of climate-induced permafrost degradation on vegetation: A review, Advances in Climate Change Research, 12, 29–47, https://doi.org/10.1016/j.accre.2020.07.002, 2021.

Jones, P. W.: First- and Second-Order Conservative Remapping Schemes for Grids in Spherical Coordinates, Mon. Weather Rev., 127, 2204–2210, https://doi.org/10.1175/1520-0493(1999)127<2204:FASOCR>2.0.CO;2, 1999.

Jordan, R. E.: A one-dimensional temperature model for a snow cover: Technical documentation for SNTHERM. 89., Cold Regions Research and Engineering Laboratory (U.S.) Engineer Research and Development Center (U.S.), https://erdc-library.erdc.dren.mil/jspui/handle/11681/11677 (last access: 8 April 2025), 1991.

Langer, M., Westermann, S., Heikenfeld, M., Dorn, W., and Boike, J.: Satellite-based modeling of permafrost temperatures in a tundra lowland landscape, Remote Sens. Environ., 135, 12–24, https://doi.org/10.1016/j.rse.2013.03.011, 2013.

Lawrence, D., Fischer, R., Koven, C., Oleson, K., Swenson, S., and Vertenstein, M.: Technical Description of version 5.0 of the Community Land Model (CLM), University Corporation for Atmospheric Research (UCAR), https://escomp.github.io/ctsm-docs/versions/master/html/tech_note/Introduction/CLM50_Tech_Note_Introduction.html (last access: 8 April 2025), 2018.

Lawrence, D. M. and Slater, A. G.: The contribution of snow condition trends to future ground climate, Clim. Dynam., 34, 969–981, https://doi.org/10.1007/s00382-009-0537-4, 2010.

Lawrence, D. M., Fisher, R. A., Koven, C. D., Oleson, K. W., Swenson, S. C., Bonan, G., Collier, N., Ghimire, B., van Kampenhout, L., Kennedy, D., Kluzek, E., Lawrence, P. J., Li, F., Li, H., Lombardozzi, D., Riley, W. J., Sacks, W. J., Shi, M., Vertenstein, M., Wieder, W. R., Xu, C., Ali, A. A., Badger, A. M., Bisht, G., van den Broeke, M., Brunke, M. A., Burns, S. P., Buzan, J., Clark, M., Craig, A., Dahlin, K., Drewniak, B., Fisher, J. B., Flanner, M., Fox, A. M., Gentine, P., Hoffman, F., Keppel-Aleks, G., Knox, R., Kumar, S., Lenaerts, J., Leung, L. R., Lipscomb, W. H., Lu, Y., Pandey, A., Pelletier, J. D., Perket, J., Randerson, J. T., Ricciuto, D. M., Sanderson, B. M., Slater, A., Subin, Z. M., Tang, J., Thomas, R. Q., Val Martin, M., and Zeng, X.: The Community Land Model Version 5: Description of New Features, Benchmarking, and Impact of Forcing Uncertainty, J. Adv. Model. Earth Sy., 11, 4245–4287, https://doi.org/10.1029/2018MS001583, 2019.

Lee, H., Swenson, S. C., Slater, A. G., and Lawrence, D. M.: Effects of excess ground ice on projections of permafrost

in a warming climate, Environ. Res. Lett., 9, 124006, https://doi.org/10.1088/1748-9326/9/12/124006, 2014.

Li, G., Zhao, Y., Zhang, W., and Xu, X.: Influence of snow cover on temperature field of frozen ground, Cold Reg. Sci. Technol., 192, https://doi.org/10.1016/j.coldregions.2021.103402, 2021.

Liu, Z., Kimball, J. S., Ballantyne, A., Watts, J. D., Natali, S. M., Rogers, B. M., Yi, Y., Klene, A. E., Moghaddam, M., Du, J., and Zona, D.: Widespread deepening of the active layer in northern permafrost regions from 2003 to 2020, Environ. Res. Lett., 19, https://doi.org/10.1088/1748-9326/ad0f73, 2024.

Matthes, H., Rinke, A., Zhou, X., and Dethloff, K.: Uncertainties in coupled regional Arctic climate simulations associated with the used land surface model, J. Geophys. Res.-Atmos., 122, 7755–7771, https://doi.org/10.1002/2016JD026213, 2017.

Mellor, M.: Engineering Properties of Snow, J. Glaciol., 19, 15–66, https://doi.org/10.3189/S002214300002921X, 1977.

Melton, J. R., Arora, V. K., Wisernig-Cojoc, E., Seiler, C., Fortier, M., Chan, E., and Teckentrup, L.: CLASSIC v1.0: the open-source community successor to the Canadian Land Surface Scheme (CLASS) and the Canadian Terrestrial Ecosystem Model (CTEM) – Part 1: Model framework and site-level performance, Geosci. Model Dev., 13, 2825–2850, https://doi.org/10.5194/gmd-13-2825-2020, 2020.

Obu, J., Westermann, S., Bartsch, A., Berdnikov, N., Christiansen, H. H., Dashtseren, A., Delaloye, R., Elberling, B., Etzelmüller, B., Kholodov, A., Khomutov, A., Kääb, A., Leibman, M. O., Lewkowicz, A. G., Panda, S. K., Romanovsky, V., Way, R. G., Westergaard-Nielsen, A., Wu, T., Yamkhin, J., and Zou, D.: Northern Hemisphere permafrost map based on TTOP modelling for 2000–2016 at $1 \, km^2$ scale, Earth-Sci. Rev., 193, 299–316, https://doi.org/10.1016/j.earscirev.2019.04.023, 2019.

Obu, J., Westermann, S., Barboux, C., Bartsch, A., Delaloye, R., Grosse, G., Heim, B., Hugelius, G., Irrgang, A., Kääb, A., Kroisleitner, C., Matthes, H., Nitze, I., Pellet, C., Seifert, F., Strozzi, T., Wegmüller, U., Wieczorek, M., and Wiesmann, A.: ESA Permafrost Climate Change Initiative (Permafrost_cci): Permafrost version 3 data products, Centre for Environmental Data Analysis [data set], http://catalogue.ceda.ac.uk/uuid/8239d5f6263f4551bf2bd100d3ecbead (last access: 8 April 2025), 2024.

Oogathoo, S., Houle, D., Duchesne, L., and Kneeshaw, D.: Evaluation of simulated soil moisture and temperature for a Canadian boreal forest, Agr. Forest Meteorol., 323, 109078, https://doi.org/10.1016/j.agrformet.2022.109078, 2022.

Osterkamp, T. E. and Romanovsky, V. E.: Evidence for warming and thawing of discontinuous permafrost in Alaska, Permafrost Periglac., 10, 17–37, https://doi.org/10.1002/(SICI)1099-1530(199901/03)10:1<17::AID-PPP303>3.0.CO;2-4, 1999.

Palmtag, J., Obu, J., Kuhry, P., Richter, A., Siewert, M. B., Weiss, N., Westermann, S., and Hugelius, G.: A high spatial resolution soil carbon and nitrogen dataset for the northern permafrost region based on circumpolar land cover upscaling, Earth Syst. Sci. Data, 14, 4095–4110, https://doi.org/10.5194/essd-14-4095-2022, 2022.

Paquin, J.-P. and Sushama, L.: On the Arctic near-surface permafrost and climate sensitivities to soil and snow model formulations in climate models, Clim. Dynam., 44, 203–228, https://doi.org/10.1007/s00382-014-2185-6, 2015.

Park, H., Fedorov, A. N., Zheleznyak, M. N., Konstantinov, P. Y., and Walsh, J. E.: Effect of snow cover on pan-Arctic permafrost thermal regimes, Clim. Dynam., 44, 2873–2895, https://doi.org/10.1007/s00382-014-2356-5, 2015.

Pongracz, A., Wårlind, D., Miller, P. A., and Parmentier, F.-J. W.: Model simulations of arctic biogeochemistry and permafrost extent are highly sensitive to the implemented snow scheme in LPJ-GUESS, Biogeosciences, 18, 5767–5787, https://doi.org/10.5194/bg-18-5767-2021, 2021.

Rawlins, M. A. and Karmalkar, A. V.: Regime shifts in Arctic terrestrial hydrology manifested from impacts of climate warming, The Cryosphere, 18, 1033–1052, https://doi.org/10.5194/tc-18-1033-2024, 2024.

Royer, A., Picard, G., Vargel, C., Langlois, A., Gouttevin, I., and Dumont, M.: Improved Simulation of Arctic Circumpolar Land Area Snow Properties and Soil Temperatures, Front. Earth Sci., 9, 685140, https://doi.org/10.3389/feart.2021.685140, 2021.

Schuur, E. A., McGuire, A. D., Schädel, C., Grosse, G., Harden, J. W., Hayes, D. J., Hugelius, G., Koven, C. D., Kuhry, P., Lawrence, D. M., Natali, S. M., Olefeldt, D., Romanovsky, V. E., Schaefer, K., Turetsky, M. R., Treat, C. C., and Vonk, J. E.: Climate change and the permafrost carbon feedback, Nature, 520, 171–179, https://doi.org/10.1038/nature14338, 2015.

Schädel, C., Rogers, B. M., Lawrence, D. M., Koven, C. D., Brovkin, V., Burke, E. J., Genet, H., Huntzinger, D. N., Jafarov, E., McGuire, A. D., Riley, W. J., and Natali, S. M.: Earth system models must include permafrost carbon processes, Nat. Clim. Change, 14, 114–116, https://doi.org/10.1038/s41558-023-01909-9, 2024.

Shiklomanov, N. I., Streletskiy, D. A., and Nelson, F. E.: Northern Hemisphere component of the global Circumpolar Active Layer Monitoring (CALM) Program, in: Proceedings of the 10th International Conference on Permafrost, edited by: Hinkel, K. M., vol. 1, Salekhard: The Northern Publisher Salekhard, 377–382, https://www.researchgate.net/profile/Nikolay-Shiklomanov/publication/303133162_Northern_Hemisphere_component_of_the_global_Circumpolar _Active_Layer_Monitoring_CALM_program/links/581b6b0b08 aea429b28fca7b/Northern-Hemisphere-component-of-the-global-Circumpolar-Active-Layer-Monitoring-CALM-program.pdf (last access: 8 April 2025), 2012.

Slater, A. G., Lawrence, D. M., and Koven, C. D.: Process-level model evaluation: a snow and heat transfer metric, The Cryosphere, 11, 989–996, https://doi.org/10.5194/tc-11-989-2017, 2017.

Sturm, M., Holmgren, J., and Liston, G. E.: A Seasonal Snow Cover Classification System for Local to Global Applications, J. Climate, 8, 1261–1283, https://doi.org/10.1175/1520-0442(1995)008<1261:ASSCCS>2.0.CO;2, 1995.

Sturm, M., Holmgren, J., König, M., and Morris, K.: The thermal conductivity of seasonal snow, J. Glaciol., 43, 26–41, https://doi.org/10.3189/S0022143000002781, 1997.

Tao, J., Zhu, Q., Riley, W. J., and Neumann, R. B.: Improved ELMv1-ECA simulations of zero-curtain periods and cold-season CH$_4$ and CO$_2$ emissions at Alaskan Arctic tundra sites, The Cryosphere, 15, 5281–5307, https://doi.org/10.5194/tc-15-5281-2021, 2021.

Tao, J., Riley, W. J., and Zhu, Q.: Evaluating the impact of peat soils and snow schemes on simulated active layer thickness at pan-Arctic permafrost sites, Environ. Res. Lett., 19, 054027, https://doi.org/10.1088/1748-9326/ad38ce, 2024.

van Kampenhout, L., Lenaerts, J. T., Lipscomb, W. H., Sacks, W. J., Lawrence, D. M., Slater, A. G., and van den Broeke, M. R.: Improving the Representation of Polar Snow and Firn in the Community Earth System Model, J. Adv. Model. Earth Sy., 9, 2583–2600, https://doi.org/10.1002/2017MS000988, 2017.

Verseghy, D. L.: Class-A Canadian land surface scheme for GCMS. I. Soil model, Int. J. Climatol., 11, 111–133, https://doi.org/10.1002/joc.3370110202, 1991.

Vionnet, V., Brun, E., Morin, S., Boone, A., Faroux, S., Le Moigne, P., Martin, E., and Willemet, J.-M.: The detailed snowpack scheme Crocus and its implementation in SURFEX v7.2, Geosci. Model Dev., 5, 773–791, https://doi.org/10.5194/gmd-5-773-2012, 2012.

Wang, T., Ottlé, C., Boone, A., Ciais, P., Brun, E., Morin, S., Krinner, G., Piao, S., and Peng, S.: Evaluation of an improved intermediate complexity snow scheme in the ORCHIDEE land surface model, J. Geophys. Res.-Atmos., 118, 6064–6079, https://doi.org/10.1002/jgrd.50395, 2013.

Wang, W., Rinke, A., Moore, J. C., Ji, D., Cui, X., Peng, S., Lawrence, D. M., McGuire, A. D., Burke, E. J., Chen, X., Decharme, B., Koven, C., MacDougall, A., Saito, K., Zhang, W., Alkama, R., Bohn, T. J., Ciais, P., Delire, C., Gouttevin, I., Hajima, T., Krinner, G., Lettenmaier, D. P., Miller, P. A., Smith, B., Sueyoshi, T., and Sherstiukov, A. B.: Evaluation of air–soil temperature relationships simulated by land surface models during winter across the permafrost region, The Cryosphere, 10, 1721–1737, https://doi.org/10.5194/tc-10-1721-2016, 2016.

Yang, K., Wang, C., and Li, S.: Improved Simulation of Frozen-Thawing Process in Land Surface Model (CLM4.5), J. Geophys. Res.-Atmos., 123, 13238–13258, https://doi.org/10.1029/2017JD028260, 2018.

Yen, Y.-C.: Review of thermal properties of snow, ice, and sea ice, vol. 81, US Army, Corps of Engineers, Cold Regions Research and Engineering Laboratory, Hanover, https://books.google.de/books?hl=en&lr=&id=fh8xryamPxIC& oi=fnd&pg=PR1&dq=yen+Review+of+thermal+properties+ of+snow,+ice,+and+sea+ice,&ots=Riw4X2_ZuW&sig= NN5HpL5DEQVsJd_lMe3_IF7IyjM&redir_esc=y#v= onepage&q=yenReviewofthermalpropertiesofsnow,ice, andseaice,&f=false (last access: 8 April 2025, 1981.

Zhao, W., Mu, C., Wu, X., Zhong, X., Peng, X., Liu, Y., Sun, Y., Liang, B., and Zhang, T.: Spatio-Temporal Characteristics and Differences in Snow Density between the Tibet Plateau and the Arctic, Remote Sens.-Basel, 15, 3976, https://doi.org/10.3390/rs15163976, 2023.